The effect of nearby fractures on hydraulically induced fracture propagation and permeability changes

Bruno Figueiredo[1], Chin-Fu Tsang[1,2], Jonny Rutqvist[2] and Auli Niemi[1]
[1]Uppsala University, Villavägen 16, Uppsala, Sweden
e-mail: bruno.figueiredo@geo.uu.se
Phone number: +46739735500
[2]Lawrence Berkeley National Laboratory, Berkeley, California

Abstract: Fracture propagation caused by a hydraulic fracturing operation can be significantly influenced by nearby fractures. This paper presents a detailed coupled hydro-mechanical analysis to study the effect of nearby fractures on hydraulically induced fracture propagation and changes in fracture permeability. Two fractured rock domains were considered in comparison: FD1, with one single fracture, and FD2, with two adjacent parallel and non-parallel fractures. It is assumed that water injection occurs in a borehole that intersects the single fracture in FD1, and one of the two fractures, in FD2. Simulations were made for a time period of 3 hours with an injection period of 2 hours followed by 1 hour of shut-in. An elastic-brittle model based on material properties degradation, was implemented in a 2D finite-difference scheme, and used for elements of the intact rock subjected to tension failure. The intact rock was considered to have a low but non-negligible permeability. A verification study against analytical solutions showed that the fracture propagation and stress concentrations due to differential boundary stresses can be accurately represented by our model. Then, a base case is considered, in which the ratio *SR* between the magnitudes of the maximum and minimum boundary stresses, the permeability k_R of the intact rock and the initial permeability k_{TF} of the tension failure regions, are fixed. In FD2, the distance *d* between the two fractures defined as the closest distance is also fixed. Results show that in both fractured rock domains, the fracture starts to propagate when the pore pressure is approximately 85% of the magnitude of minimum boundary stress. The propagation of a single fracture is significantly larger than the propagation of a double fracture system, because in the latter case, the pore pressure decreases when the two fractures connect. As a result, changes in permeability in FD2 were found to be smaller than in FD1. At 2 hours of injection the maximum ratio between the final and initial permeability of the fractures was found to be approximately 3 and 2 for fractured rock domains FD1 and FD2, respectively. For non-parallel fractures, the controlling factor is the separation between the tips of pressurised fracture to the neighbouring non-pressurised fracture. A sensitivity analysis was done to study the influence of the key parameters *d*, *SR,* k_R and k_{TF} on the simulation results. Fracture propagation showed more sensitivity to *d* and *SR* than to the other parameters.

Keywords: hydraulic fracturing stimulation, coupled hydro-mechanical effects, fractures propagation and connectivity, elastic-brittle model

1. INTRODUCTION

Hydraulic fracturing is a method used routinely in oil and gas exploitation and in enhanced geothermal systems. This is a technique which creates fractures in deep-rock formations by mean of high pressure fluid injection and thus increases flow permeability in the injection region. Hydraulic fracturing stimulation leads to changes in pore pressure and effective normal stress across the created fractures, which in turn, leads to consequent fracture propagation. Hence, the fracture permeability depends on the *in situ* stress conditions and on the pressure of the flowing fluid [1]. Hydro-mechanical coupling is an important issue that needs to be taken into account [2,3].

In order to understand the fracturing processes, several laboratory experiments and 2D and 3D numerical studies have been made by many researchers. In those studies, the fracture closure, extension and mechanical interactions for parallel and quasi-parallel fractures have been analysed [4, 5, 6]. Laboratory experiments were done in gypsum ([7], [8]) and gympsum and marble ([9], [10]) to understand the fracture propagation caused by differential boundary stresses. In [11] and [12], samples of granite with single and double flaw geometries under quasi-static vertical compressive loads were tested. In [13] fractures were created by compressing granite cores uniaxially. In [14] the fracture propagation in sandstones induced by the confining stresses and increase pore pressure was studied. Fracture propagation based on application of dynamic loads was studied in [15], [16] and [17].

Numerical continuum and discrete based models have been developed to study the fracture propagation induced by hydraulic injection pressure under confining stresses. Continuum based models have used the finite element method ([18], [19], [20], [21], [22]), the extended finite element method ([23], [24], [25], [26]) and the explicit finite differences method ([27], [28], [29]). Discrete based models used the boundary element method ([30], [31], [32]), the particle flow method ([33], [34], [35], [36], [37]), the bonded particle model ([38]), the distinct element code ([39]) and the discontinuum deformation analysis method ([40]).

Discrete based models are more realistic for discontinuous media, but they have the limitation of not considering the intact rock permeability and are time consuming for modelling the hydro-mechanical behaviour of fractured rock domains with curved or dead-end fractures. Continuum based models require a representation of discrete fracture behaviour in an element cell by appropriate equivalent hydro-mechanical properties [41]. Compared with discontinuous approaches, they have as main advantages, the representation of complex fracture networks without the need of update their topology and the modelling with high accuracy of the hydro-mechanical behaviour of both rock matrix and the fractures which can be sealed or filled with mineral materials. Thus, once the fracture propagates into the continuum medium, stress-induced changes in permeability and porosity can be included ([42], [43], [44], [45], [46]). By using an elastic-plastic and strain softening model, a continuum based model may not be very effective in simulating fracture propagation because of large plastic zones around the fracture tips. However, it has been shown that a model based on degradation of the mechanical properties and stress distribution for the failure elements of the intact rock by tension and shear, is effective for this purpose ([27], [28], [29]).

To the authors' knowledge, no continuum based model was used in a detailed coupled hydro-mechanical study to understand the difference between the propagation in a low permeable medium of a single fracture and double parallel and non-parallel fractures under various stress conditions and different levels of fluid injection pressure. For our study of coupled hydro-mechanical effects as a function of increases in pore pressure, we consider two fractured rock domains: the first with one single fracture, and the second with double adjacent parallel and non-parallel fractures. Changes in fluid pore pressure are assumed to be caused by constant injection flow rate in a well that intersects one of the fractures.

The main objectives of the paper are (1) firstly to verify or demonstrate the effectiveness of using a continuum mechanics based model with an implemented elastic-brittle stress relation to simulate the fracture propagation and stress concentrations around fracture tips, (2) to study how a single fracture propagates when it is subjected to hydraulic fracturing stimulation (3) to evaluate changes in the pore pressure field and fracture permeability induced by coupled hydro-mechanical processes (4) to analyse how the results are influenced by a nearby parallel and non-parallel fracture and (5) to conduct a sensitivity analysis to determine the key parameters with significant influence on fracture propagation and linkage between nearby fractures during hydraulic fracturing process. The paper is completed with some concluding remarks.

2. PROBLEM DEFINITION

For our study, we choose to consider two fractured rock domains, FD1 and FD2, each with dimensions 50 m × 50 m, which allow us to conduct a large number of simulations in order to explore the detailed coupled hydro-mechanical processes involved. The fractured rock domains FD1 and FD2 consider one single and two fractures, respectively (Fig. 1). In FD2, the left and right hand-side fractures are identified as fractures 1 and 2. In both rock domains, the length *2f* of the fractures is 2 m.

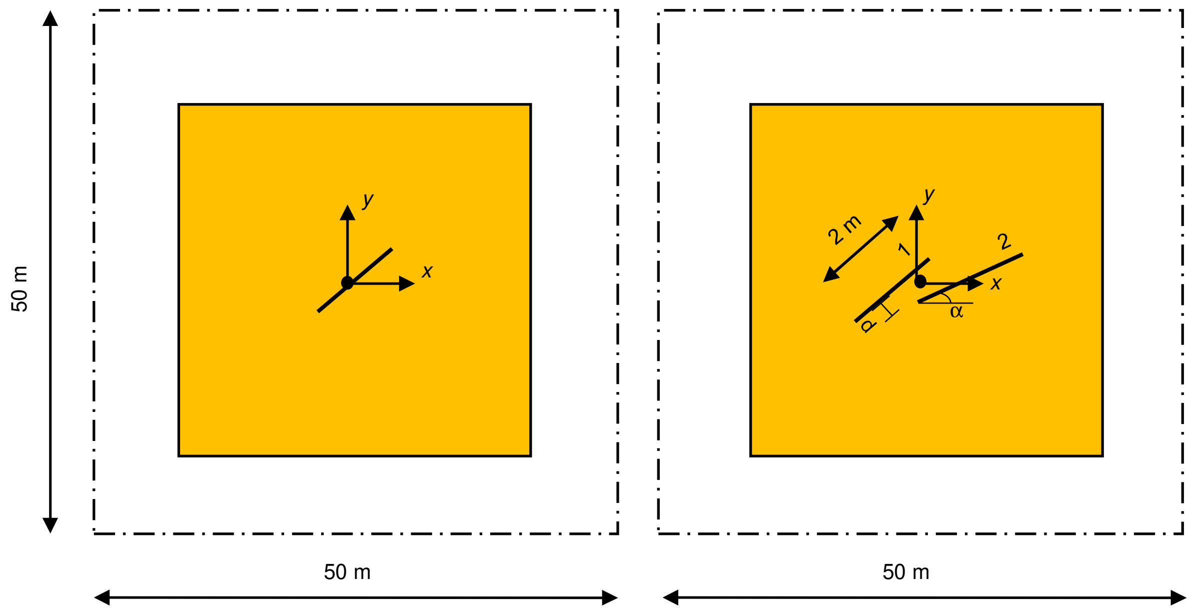

Fig. 1: Geometry of the fractured rock domains FD1 (left) and FD2 (right)

To study in detail the linkage between the two fractures, in FD2, parallel and non-parallel fractures with different angles between those and the maximum horizontal boundary stress direction, were considered. Thus, for parallel fracture case, the fractures were assumed to be at angles α_1 and α_2 equal to 30°, 45° and 60°, and for non-parallel fracture case, the angle α_1 of fracture 1 is taken to be equal to 45°, and the angle α_2 of fracture 2 to be equal to 30° and 60°. The origin of the *x* and *y*-axis system is located in the centre of the studied regions. In FD2, the closest distance *d* (see Fig. 1) between the fractures is 0.25 m, with a sensitivity analysis conducted to study the influence of *d* on the obtained results (see section 6.1).

Let us now assume that these fractured rock domains are located at 1000 m depth. By assuming a vertical gradient of 0.027 MPa/m, the magnitude of the vertical stress component (S_v) at 1000 m depth below the surface is 27 MPa. A loading case was considered, in which the minimum horizontal boundary stress magnitude (S_h) is equal to the vertical stress magnitude (σ_v) and the ratio *SR* between the maximum horizontal S_H and minimum horizontal S_h boundary stresses is 2 (Fig. 2). Further, a sensitivity analysis is made to study the influence of *SR* on the simulation results (see section 6.2). Because the vertical dimension of the model is only 50 m, the vertical gradient of all stress components was neglected. The stresses are applied normal to the boundaries which are free to move. No shear stresses are considered at the boundaries (see Fig. 2). Results of our simulations showed that because the boundary conditions are imposed far enough, they do not influence the stresses around fractures as well as their propagation in the intact rock.

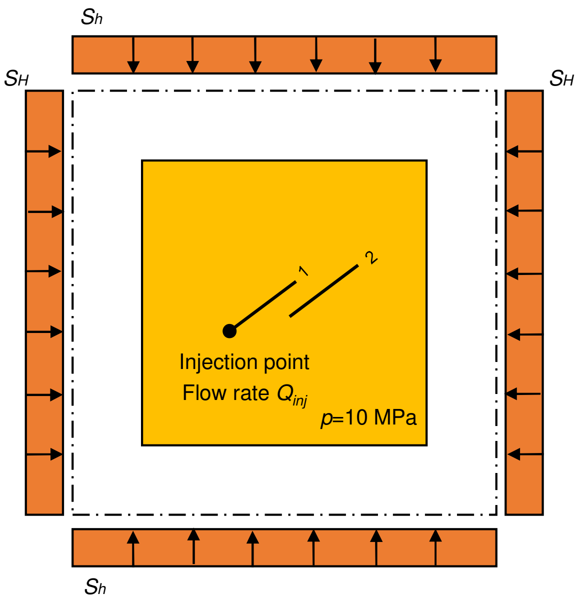

Fig. 2: Boundary loading and pore pressure conditions: S_H and S_h are the maximum and minimum horizontal boundary stresses, respectively; *p* is the initial fluid pore pressure; Q_{inj} is the constant flow rate

By assuming that the water table is located at the land surface and a fluid pore pressure vertical gradient of 0.01 MPa/m, the fluid pore pressure *p* at 1000 m depth below the surface is 10 MPa. The pore pressure gradient in the x and y-axis directions was neglected. All the boundaries were considered to be closed to flow. Results of our simulations showed that the results are not influenced by the flow boundary conditions.

We simulate a water injection at a constant rate Q_i for two hours in one borehole penetrating the only fracture in FD1 and the fracture 1 in FD2 (see Fig. 2). The borehole is assumed to be vertical (perpendicular to FD1 and FD2). In this way, hydraulic fracturing was imposed in the single fracture in FD1 and in the fracture 1 in FD2. After two hours, water injection is stopped, and the simulation continues for another hour.

3. NUMERICAL APPROACH

3.1 Finite-difference numerical model

To study the fracture propagation due to coupled hydro-mechanical effects as a result of hydraulic fracturing stimulation, a 3D model is desirable if at all possible. However a global 3D model would be very large and the necessary fine refinement close to the fracture would require a great computational effort. A 2D model is adequate from a mechanical perspective, particularly for investigating the fracture propagation, because this is driven by the pore pressure build-up at the tip of the fractures that can be simulated explicitly with a 2D model and an adequate injection rate. This should lead to a pore pressure at the fracture tip necessary to start fracture propagation, as observed in field experiments. A 2D finite-difference model was developed in FLAC3D ([47]). This code was chosen because we want to have the possibility to consider multi-phase flow in the future studies, and we have already the routines to couple FLAC3D with TOUGH2 [48], which is a leading multiphase flow and transport simulator. The model is a square region with 50 m side, with a thickness of 1 m (Fig. 3). A plane strain analysis was carried out. The mesh consists of 56000 elements and is more refined in a square region 10 m by 10 m around the fractures, where the elements are squares with each side 0.05 m (Fig. 3).

Fractures can be modelled as an equivalent solid material, in which the elastic modulus E_F of the elements intersected by a fracture trace is calculated according with the following equation ([41], [49]):

$$\frac{1}{E_F} = \frac{1}{E_R} + \frac{1}{k_n d}, \qquad (1)$$

where d is the element size (0.05 m).

The hydraulic behaviour of the fractures may be described in terms of the flow transmissivity and the normal and shear stiffness of the fractures. Laboratory experiments on single fractures show that the fracture transmissivity can be very sensitivity to changes in stress normal to the fractures as well as to shear displacement. Thus, mechanically induced changes in the fracture´s ability to conduct fluid may be estimated using the cubic relations between flow along an open fracture and fractures aperture ([2], [50]):

$$T = \frac{b_h^3 \rho g}{12\mu}, \tag{2}$$

where T is the fracture transmissivity, b_h is fracture aperture, ρ and μ are fluid density and viscosity, respectively, and g is the acceleration of gravity.

The permeability k_F of an element containing by a fracture trace is related to the fracture aperture b_h by the cubic law:

$$k_F = \frac{b_h^3}{12d}, \tag{3}$$

where d is element size (0.05 m).

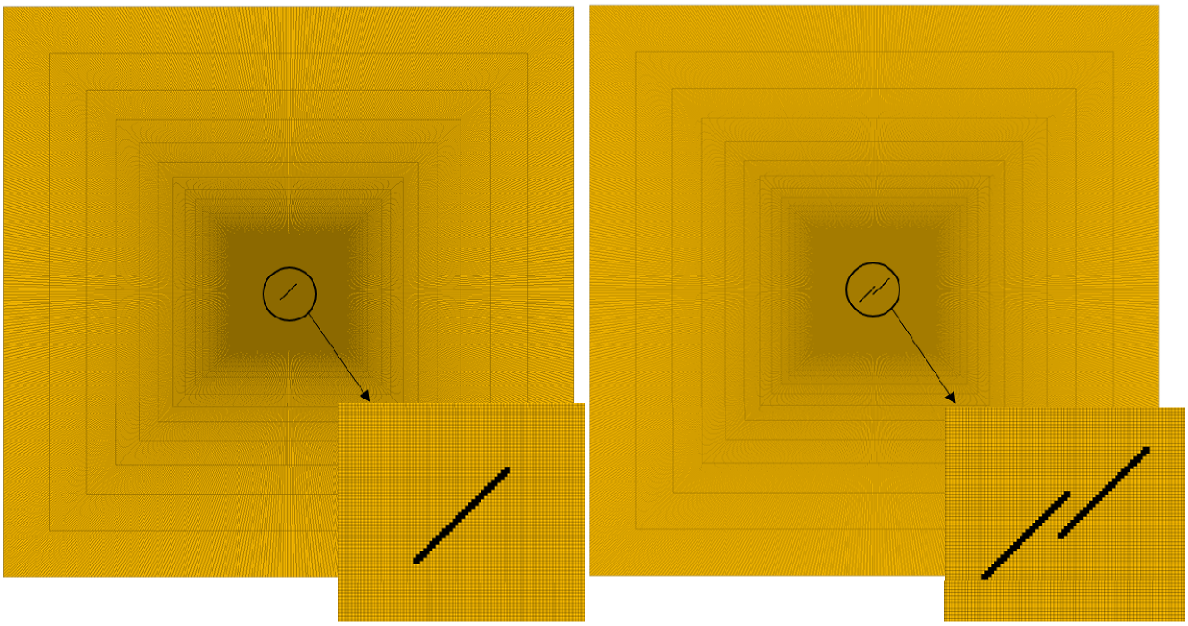

Fig. 3: Detail of the mesh of the finite-difference model to study the hydro-mechanical behaviour of the fractured rock domains FD1 (left) and FD2 (right), for the case of parallel fractures

3.2 Model parameters

Necessary model parameters are listed in Table 1. For the intact rock, a Mohr-Coulomb model with tension cut-off was used, in which the mechanical properties (elastic modulus E_R, Poisson's ratio ν_R, cohesion c_R, friction angle ϕ_R) are characteristic of limestone rocks ([51], [52]). An elastic-brittle model was implemented in FLAC3D to describe the behaviour of the failure elements in the intact rock. This model is described in the next section. A tensile strength σ_{tR} of 5 MPa for the intact rock was assumed. In the regions of the intact rock where the tensile stress exceeds the tensile strength, tension failure occurs. A sensitivity analysis was done to study the influence of this parameter on the results. An additional value of 10 MPa was considered which is acceptable for intact limestone at 1000 m depth. Results showed a decreased fracture extension when the tensile strength increases. It was found that when the tensile strength increases from 5 to 10 MPa, in FD1 the fracture propagation decreases 0.7 m. In FD2, this decrease is 10 cm and 25 cm, for fractures 1 and 2, respectively. However, the conclusions are similar to those reported in this paper. Regarding the hydraulic properties, the values of 10^{-18} m^2 and 0.001 were assigned to the permeability k_R and porosity e_R of the intact rock, which are typical of limestone rocks. Further, a sensitivity analysis is done to evaluate the influence of the permeability of intact rock on the simulation results (see section 6.3).

Table 1: FLAC3D model parameters

Intact rock	Elastic modulus E_R (GPa)	20
	Poisson´s ratio ν_R	0.2
	Tensile strength σ_{tR} (MPa)	5
	Cohesion c_R (MPa)	30
	Friction angle ϕ_R (°)	25
	Permeability k_R (m^2)	10^{-18}
	Porosity e_R	0.001
Fractures	Elastic modulus E_F (GPa)	14.3
	Poisson´s ratio ν_F	0.2
	Tensile strength σ_{tF} (MPa)	0
	Friction angle ϕ_F (°)	25
	Dilation angle ψ_F (°)	5
	Normal stiffness k_n (GPa/m)	1000
	Cohesion c_F (MPa)	0
	Aperture b_h (μm)	30
	Permeability k_F (m^2)	4.5×10^{-14}
	Porosity e_F	0.01

The mechanical fracture behaviour is modelled with continuum elasto-plasticity using a Mohr-Coulomb constitutive model with tension cut-off. The mechanical properties of the fractures (Poisson's ratio ν_F, friction angle ϕ_F, dilation angle ψ_F, cohesion c_F, fractures aperture b_h) were extracted from [1]. When the Mohr-Coulomb criterion is exceeded, plastic shear strain (and corresponding shear displacement) occurs along the fractures. The tensile strength σ_{tF} for fractures was assumed to be zero. Results of our simulations showed low sensitivity to this parameter, because tension failure occurs in the intact rock and in the fractures, shear failure is the dominant mechanism. The fracture normal stiffness k_n was assumed to be 1000 GPa/m ([49]). Based on a fractures aperture of 30 μm (see Table 1), Eqs. (2) and (3) lead to a fracture transmissivity T of 2.2 $\times10^{-8}$ m^2/s and permeability of fractures k_F of 4.5×10^{-14} m^2, respectively. The porosity e_F of an element representing a fracture was assumed to be equal to 0.01 ([49]).

In the theoretical study presented in this paper, we simulated water injection as representative of conditions that lead to propagation of existing fractures. We assumed a 2D injection rate of about 4.0 $\times 10^{-4}$ m^3/s into a 0.0025 m^3 grid block. This pressurization rate enables to reach to a maximum injection pressure that is about 2.5 times the initial pore pressure.

3.3 Elastic-brittle model in the failure regions in the intact rock

The behaviour of the intact rock undergoing tension or shear failure may be simplified to be represented by an elastic-brittle, elastic-strain softening (a combination of brittle and ductile) or elastic-ductile (plastic) mechanisms. An elastic-plastic and strain softening model cannot effectively simulate the fractures propagation because a large plastic zones appear around the fracture tips. An elastic-brittle stress-strain relation, based on degradation of the mechanical properties and consequent stress distribution for the failure elements by tension and shear (Fig. 4) has been shown to be more effective for this purpose ([27], [28], [29]). In this model, failure of an element causes disturbance of the local stress field, which may lead to progressive failure of surrounding elements.

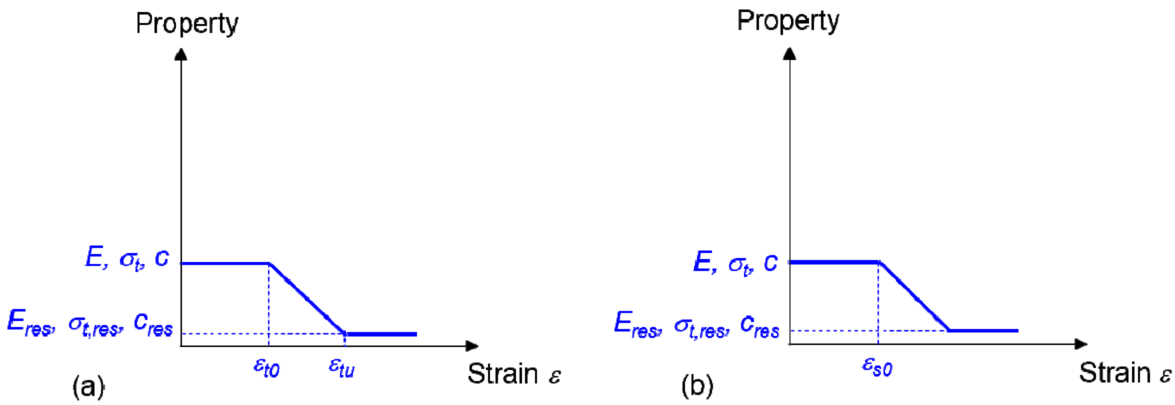

Fig. 4: Degradation of the stiffness and strength properties for the failure elements of the intact rock by (a) tension and (b) shear: E, σ_t and c are the initial values for elastic modulus, tensile strength and cohesion, respectively; E_{res}, $\sigma_{t,res}$ and c_{res} are their residual values, respectively, ε_{t0} is the strain threshold of tension damage, ε_{tu} is the limit strain of tensile strength and ε_{s0} is the strain threshold of shear damage.

In this model, for the elements in the intact rock that undergo yield tensile strength (Fig. 4a), stiffness and strength properties are degraded, according to a damage variable D. This variable can be expressed by the following equations ([29]):

$$D = \begin{cases} 0, \varepsilon < \varepsilon_{t0} \\ 1 - \dfrac{\sigma_{t,res}}{E \cdot \varepsilon}, \varepsilon_{t0} \le \varepsilon \le \varepsilon_{tu} \\ 1, \varepsilon > \varepsilon_{tu} \end{cases}, \quad (4)$$

$$\sigma_{t,res} = \eta \sigma_t , \tag{5}$$

$$\varepsilon = \sqrt{(\varepsilon_1)^2 + (\varepsilon_2)^2 + (\varepsilon_3)^2} , \tag{6}$$

where $\sigma_{t,res}$ is the residual tensile strength, E and σ_t are the elastic modulus and tensile strength of the intact rock (Table 1), η is the residual strength coefficient, ε_{t0} is the initial damage threshold, ε_{tu} is the limit of tensile strength, and ε_1, ε_2 and ε_3 are the three principal strains.

For the elements subjected to shear failure (Fig. 4b), the damage variable D can be expressed as follows ([29]):

$$D = \begin{cases} 0, \varepsilon_s < \varepsilon_{s0} \\ 1 - \dfrac{\tau_{s,res}}{\varepsilon_s \cdot E}, \varepsilon_s \geq \varepsilon_{s0} \end{cases} , \tag{7}$$

where E is the elastic modulus, $\tau_{s,res}$ is the residual strength of shear damage, ε_{s0} is the strain threshold of shear damage, and ε_s is the shear strain.

This model was implemented in a finite difference scheme. In our case, it was found that shear failure does not occur in the intact rock where tension failure is the dominant mechanism. In those regions, the stiffness and strength properties were degraded. Stiffness degradation is implemented by simply updating elastic modulus E in the stress-strain calculations, and strength degradation is modelled by reducing the tensile strength σ_t and the cohesion c of the intact rock. The friction angle was kept invariant ([29]). The corrected values for the elastic modulus E_{corr}, tensile strength $\sigma_{t,corr}$ and cohesion c_{corr} are given by the following equations:

$$E_{corr} = E - (E - E_{res}) \times D , \tag{8}$$

$$\sigma_{t,corr} = \sigma_t - (\sigma_t - \sigma_{t,res}) \times D , \tag{9}$$

$$c_{corr} = c - (c - c_{res}) \times D , \tag{10}$$

where E_{res}, $\sigma_{t,res}$ and c_{res} are the residual values of the elastic modulus, tensile strength and cohesion (Fig. 3), respectively. In our simulations, the initial values of the elastic modulus, tensile strength and cohesion (Table 1) were reduced to one percent of the original values ([29]). This enabled our model to obtain a good fit for fracture extension with the analytical solutions when the rock domain is subjected to differential boundary stresses, as it will be shown in section 4.

In the original fractures, shear failure is the dominant mechanism. The elements that represent them get into shear failure for very small shear strains because they have null cohesion. Consequently, for those elements, the stiffness is not degraded and the elastic modulus is given by equation (1).

3.4 Permeability changes in the natural fractures and tension failure regions

In fractured rock masses, effective stresses (which include effect of fluid pore pressure) induce changes in hydraulic properties, such as the permeability and porosity. In natural fractures the initial values of porosity and permeability were corrected by taking into account changes in volumetric strains ([50]), which are defined as the ratio of the change in volume of the fracture elements to its original volume. For this purpose, a model developed and applied by [53] to consider permeability changes in petroleum reservoirs was used. This model first relates the porosity ϕ at a given stress to the isotropic volumetric strain variation ε_v in the fracture elements and then the permeability k at a given stress to changes in porosity, according to the following equations:

$$\phi = 1 - (1 - \phi_i)\exp(-\varepsilon_v), \tag{11}$$

$$k = k_i \left(\frac{\phi}{\phi_i} \right)^n , \tag{12}$$

where ϕ_i is the initial porosity, k_i is the initial permeability and n is a power law exponent.

With the changes in volumetric strains resulting from changes in the fractures normal stress, changes in fractures aperture are considered: if the compressive stress normal to the fractures decreases, the fractures aperture increases and the compressive volumetric strains decrease. Volumetric strains include elastic and plastic components. Elastic component is originated by elastic shear deformation until the Mohr-Coulomb criterion is reached. After this criterion is reached, shear failure occurs and variations in the volumetric strains include effects of plastic shear deformation and associated shear dilation. Shear dilation leads to an increase in the fractures aperture and a subsequent increase in the initial values of porosity and permeability of the fractures.

The empirical relation between permeability and porosity expressed in Eq. (12) has been shown to be widely applicable to geological materials. Even though the exponent n could vary between 3 and 25 for consolidated geological materials ([54]), we have set the exponent to 3, based on a cubic variation of the permeability with the aperture and porosity of the elements intersected by the fracture trace ([55]):

$$\frac{k}{k_i} = \left(\frac{b_h}{b_{hi}} \right)^3 = \left(\frac{\phi \cdot d}{\phi_i \cdot d} \right)^3 = \left(\frac{\phi}{\phi_i} \right)^3 , \tag{13}$$

where b_{hi} is the initial aperture of the fractures.

The failure regions by tension in the intact rock are considered to be similar to natural fractures. When the elements of the intact rock get into failure by tension, they are assigned with the same initial values for porosity and permeability as those of natural fracture elements. Then, these initial values were updated, according to Eqs. (11) and (12), to take into account the stress induced changes in porosity and permeability ([50]). In this way, extension of fractures is modelled. It was found that the maximum increase in the initial permeability of the tension failure regions is two orders of magnitude. Further, a sensitivity analysis is done to evaluate the influence of the permeability of the tension failure regions on the obtained results (see section 6.4).

3.5 Coupled hydro-mechanical calculation

A mechanical analysis is carried out by considering the boundary stresses S_H and S_h and the initial fluid pore pressure p of 10 MPa. After the mechanical equilibrium is reached, a flow analysis is made to calculate changes in pore pressure field resultant from water injection into the fracture (see Fig. 2) with a constant flow rate Q_{inj} during a 2 hours period. At 2 hours of injection, water injection is stopped. Increase in fluid pore pressure in the fracture and surrounding intact rock leads to a decrease in the effective stress. In the regions of intact rock where the tensile stresses exceed the tensile strength, tension failure occurs. Then, a mechanical analysis is made to calculate stress field induced changes in porosity and permeability. The post-failure values of porosity and permeability of those tension failure regions are set to the respective values considered for natural fractures. Then, changes in porosity and permeability in the natural fractures and tension failure regions were considered as a function of the volumetric strains, as described in section 3.4. The coupled hydro-mechanical analysis is sequential and stepped forward in time. In each time step of transient flow calculation, a quasi-static mechanical analysis is conducted to calculate stress-induced changes in permeability. The analysis is done for a period of 3 hours (shut-in occurs after 2 hours of injection).

4. VERIFICATION OF THE MODEL DUE TO MECHANICAL LOADING

To check if this model enables to simulate properly the fractures propagation in intact rock due to differential boundary stresses, the fractured rock domain FD1 was considered. For intact rock, model parameters presented in Table 1 were used. It was assumed that the fracture has no filling material and is completely open with no fracture surface contacts (no stiffness or stress transfer through surface contacts). The compressive maximum boundary stress S_H is 40 MPa (see Fig. 2), and the ratio SR between the maximum horizontal S_H and minimum horizontal S_h boundary stresses was considered to have four alternative values: 4, 5, 6.7 and 10. Fig. 5 shows the fracture propagation obtained with the FLAC3D model. Results obtained with different degrees of refinement showed that the fracture propagation trajectories are not mesh dependent. The figure shows that as expected the fracture propagation increases with the ratio between the maximum and minimum boundary stresses. At the tip of natural fractures, the fracture propagation is not confined to a single row of fractures, because of formation of wing cracks. At a certain distance away from the fracture tips, the fracture propagates in a direction perpendicular to the minimum principal stress direction. These results for fracture propagation were verified against those estimated by analytical solutions obtained for an infinite elastic medium ([56]). Fig 6 shows a comparison of the length *w* of the fracture extension (wing cracks by tension), normalised by the half-length *f* of the fracture, obtained with FLAC3D and that obtained with analytical solutions. Results of this comparison showed that the difference between the solution provided by analytical solutions and FLAC3D is reasonable with the largest difference at *SR* equal to 10, but it is smaller than 15 cm, which is acceptable for this very high stress ratio, where the fracture propagation is approximately 1 m. Additional values of 100 and 500 GPa/m were considered for the fracture normal stiffness k_n. An additional value of 10 MPa was considered for the tensile strength of σ_t. For mechanical loading, results showed low sensitivity for these two parameters.

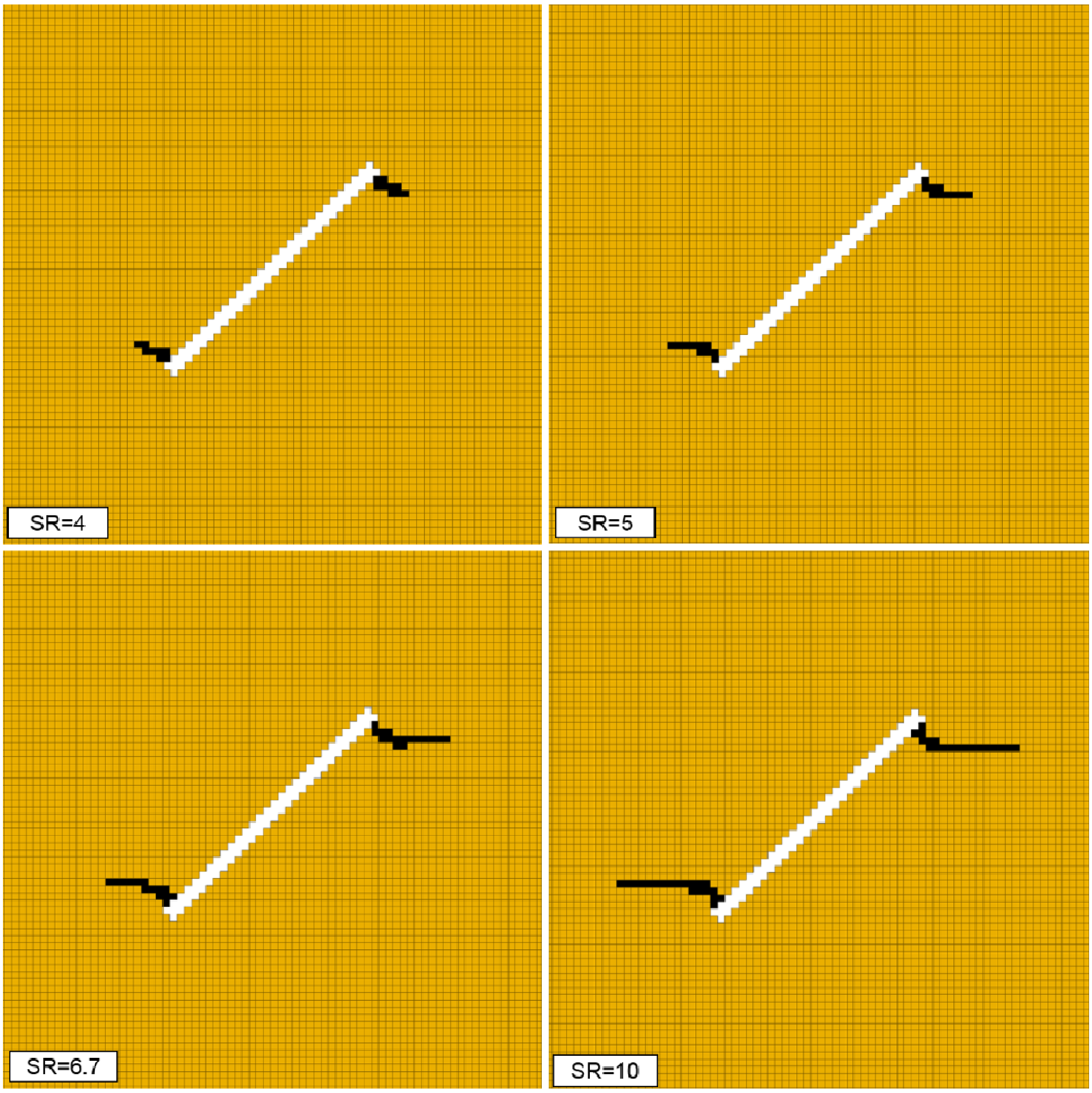

Fig. 5: Results for the fractures propagation obtained with the FLAC3D model

To check if the mesh resolution is sufficient to obtain a good estimate of the stresses close to the fractures obtained in elastic regime, a very simple model with one vertical fracture and with a length *2f* of 2 m, was considered. A stress S_H of 40 MPa was applied in the boundaries perpendicular to the x-axis (Fig. 7a). The variation of the ratio between fracture normal stress σ_{xx} and boundary stress S_H as a function of distance *r*/*2f* along the lines *x*=0 and *y*=0 away from the fracture was obtained and compared with the analytical solution presented in [57]. Results of this comparison are shown in Fig. 7b. The figure shows that, even close to the fracture, the difference between the solution provided by [57] and FLAC3D is smaller than 5%, which enables us to conclude that the calculated stress redistribution and concentrations around fractures are accurately represented in our model.

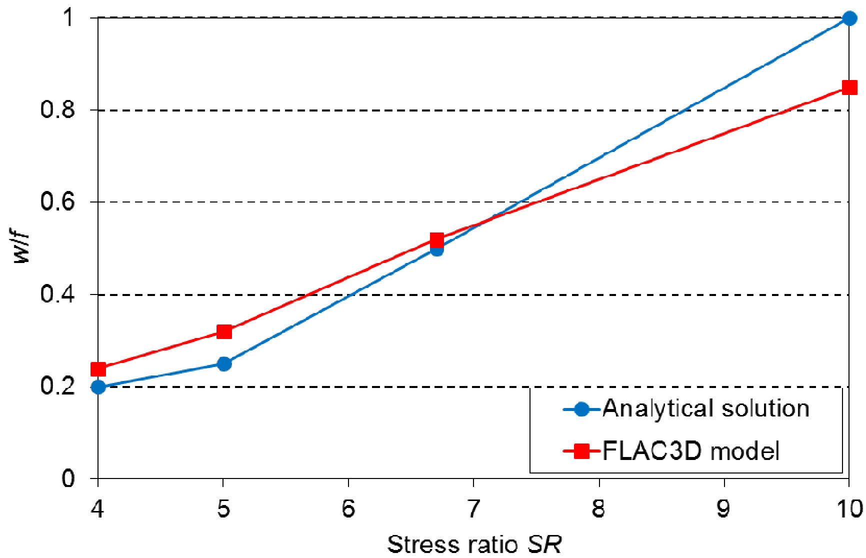

Fig. 6: Variation of the dimensionless length *w*/*f* of the tension cracks as a function of the stress ratio *SR* between the maximum horizontal S_H and minimum horizontal S_h boundary stresses

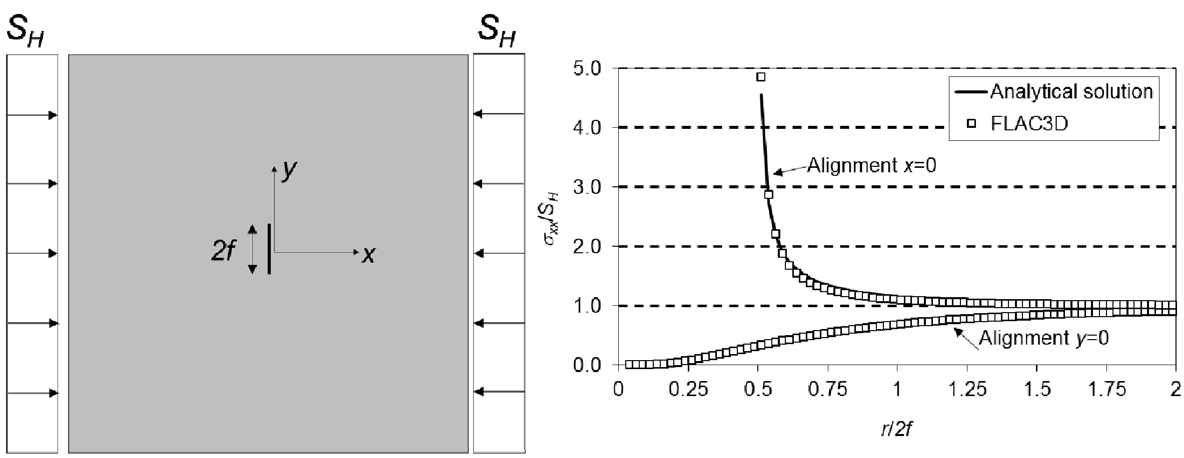

Fig. 7: (a) Geometry and boundary conditions of the model used to study the behaviour of a single fracture with length *2f* (b) variation of the fracture normal stress as a function of the distance *r* away from the fracture, along the lines *x*=0 and *y*=0

In contrast to this verification study, for our present investigation, fractures with filling material or with stress transfer through surface contacts were considered. This is a more realistic scenario because it enables the possibility considering changes in fractures aperture caused by changes in the stress normal to the fractures.

5. RESULTS

In this section, results on tension failure regions, changes in fluid pore pressure, and in fracture permeability are presented for a base case, in which the ratio *SR* between the magnitudes of the maximum and minimum boundary stresses, the permeability k_R of the intact rock, the initial permeability k_{TF} of the tension failure regions and the closest distance *d* between fractures in FD2, are fixed. A sensitivity study to analyse the influence of these key parameters on the simulation results, is presented in section 6.

5.1 Results for tension failure regions

Fig. 8 shows the failure regions by tension in the intact rock for fractured rock domains FD1 and FD2, obtained at 1.5, 2 and 3 hours for fracture angles $\alpha_1=\alpha_2=45°$. An interesting aspect is that the ratio of 2 between the magnitudes of boundary stresses is too small to lead to formation of wing cracks from mechanical effect alone, as it is observed in Fig. 5. In addition, in our study, the fractures have stiffness or shear transfer through fracture surface contacts, and consequently their extension is parallel to the maximum principal stress direction from the moment of crack initiation, as it is shown by [31]. At 1.5 and 2 hours of injection, results show that in FD1, the fracture extension is approximately 0.35 and 1.75 m, respectively. In FD2, fractures 1 and 2 (see Fig. 1) are already connected at 1.5 hours of injection. At 2 hours of injection, their extension (away from the connected region) is 35 cm which is significantly smaller than in FD1. In addition, fracture 1 does not extend beyond fracture 2. This is because in FD2, when the two fractures connect, the pore pressure decreases and becomes smaller than the minimum pressure necessary to initiate the propagation of the fracture (see section 5.2). In FD1, at 3 hours, the fracture propagates approximately 2.25 m longer and is still propagating. In FD2 case, the two fractures only propagate 0.15 m after the shut-in at 2 hours of injection. This is because in FD1 the fluid pore pressure is larger than in FD2. This will be explained with more detail in the next section.

Let us now consider the fractured rock domain FD2 and the 2 hours of injection period. Fig. 9 shows those failure regions for parallel fractures inclined at angles $\alpha_1=\alpha_2=30°$ and $\alpha_1=\alpha_2=60°$ and non-parallel fractures inclined at angles $\alpha_1=45°$, $\alpha_2=30°$ and $\alpha_1=45°$, $\alpha_2=60°$. Results obtained for parallel fractures with $\alpha_1=\alpha_2=30°$, the extension of both fractures (away from the connection zone) is 30 cm, which is less 5 cm that that obtained for fracture angles $\alpha_1=\alpha_2=45°$. When $\alpha_1=\alpha_2=60°$, the fractures do connect but their propagation is small because for this geometry, the fractures are sub-perpendicular to the horizontal direction, which is the maximum principal stress direction. For the non-parallel fractures case, when α_2 decreases from 45° to 30°, the extension (away from the connected region) of the pressurized fracture (fracture 1) increases approximately 0.5 m. When α_2 increases from 45° to 60°, that fracture extension decreases approximately 0.4 m. For α_2 equal to 60°, the non-pressurised fracture (fracture 2) does not propagate. The justification will be explained in sections 5.2 and 5.3.

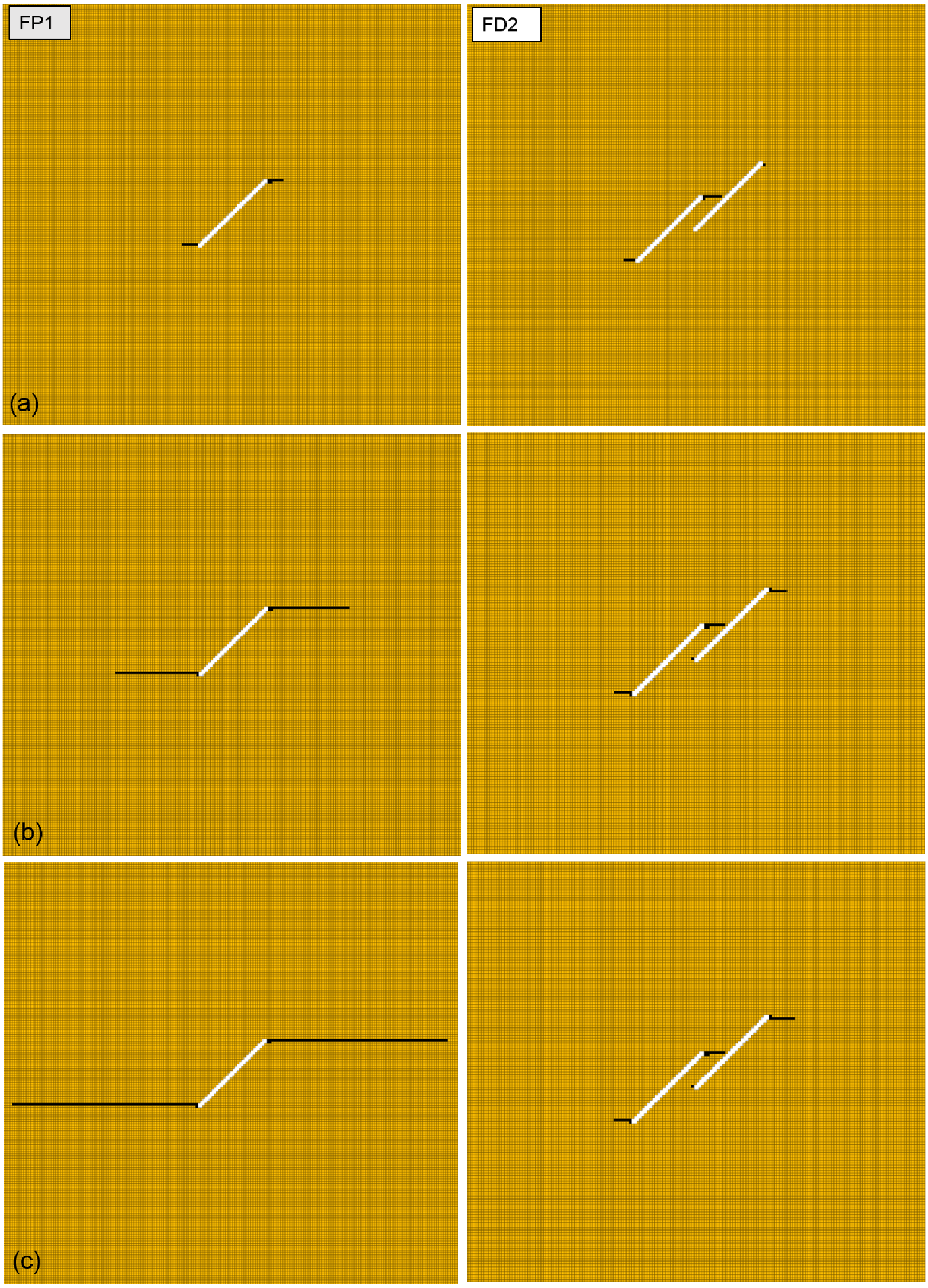

Fig. 8: Tension failure regions in fractured rock domains FD1 (left) and FD2 with parallel fractures (right) at (a) 1.5 hours (b) 2 hours and (c) 3 hours (results obtained for fracture angles $\alpha_1=\alpha_2=45°$)

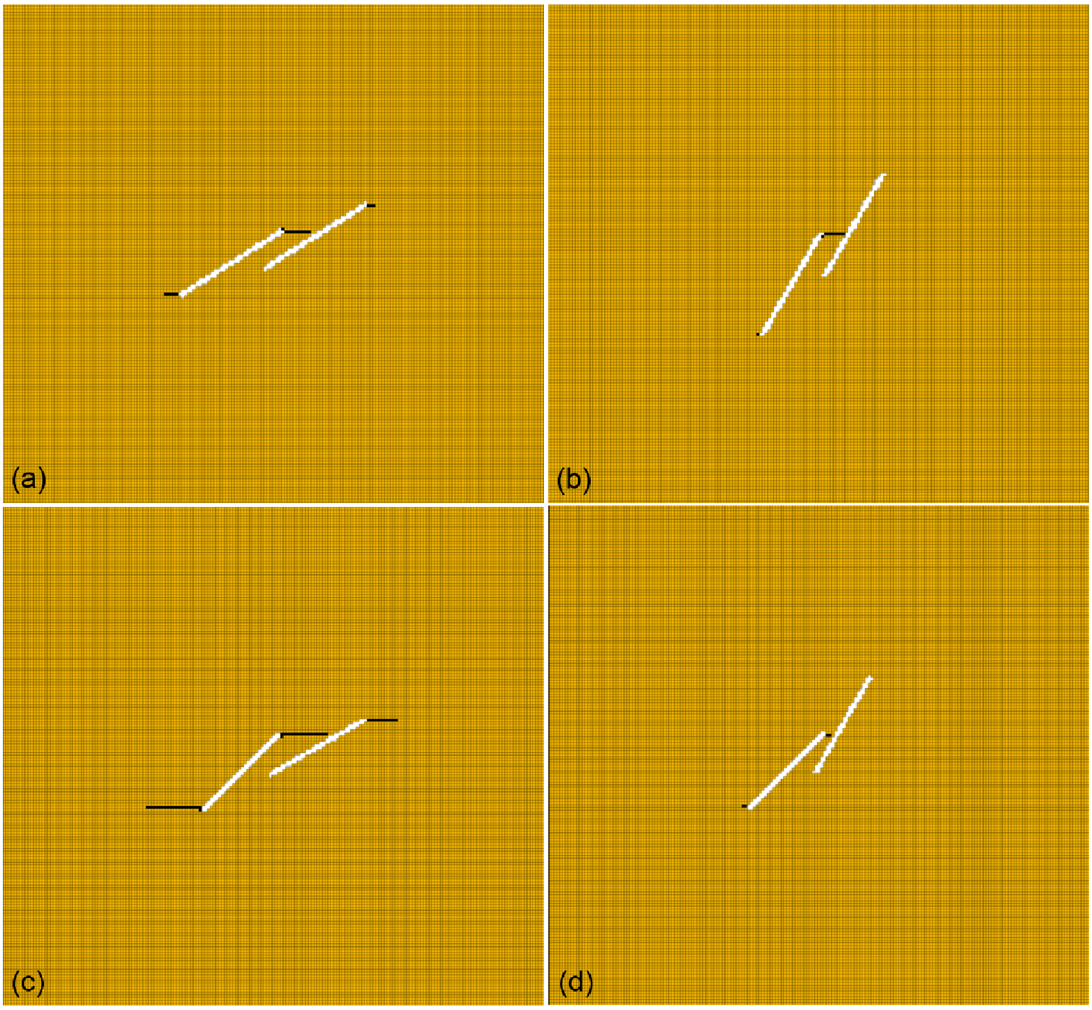

Fig. 9: Tension failure regions in fractured rock domain FD2 for fracture angles (a) $\alpha_1=\alpha_2=30°$ (parallel) (b) $\alpha_1=\alpha_2=60°$ (parallel) (c) $\alpha_1=45°$, $\alpha_2=30°$ (non-parallel) (d) $\alpha_1=45°$, $\alpha_2=60°$ (non-parallel) (results obtained at 2 hours of injection)

5.2 Changes in fluid pore pressure

In this section, changes in the fluid pore pressure due to coupled hydro-mechanical effects are analysed. Fig. 10 shows the contour of the fluid pore pressure field obtained in fractured rock domains FD1 and FD2 after 1.5 hours, 2 hours (end of injection) and 3 hours (after 1 hour of shut-in), when the two fractures are parallel and have angles $\alpha_1=\alpha_2=45°$. Fig. 11 shows the variation of the fluid pore pressure with time in the centre of the fractures for the fractured rock domains FD1 and FD2.

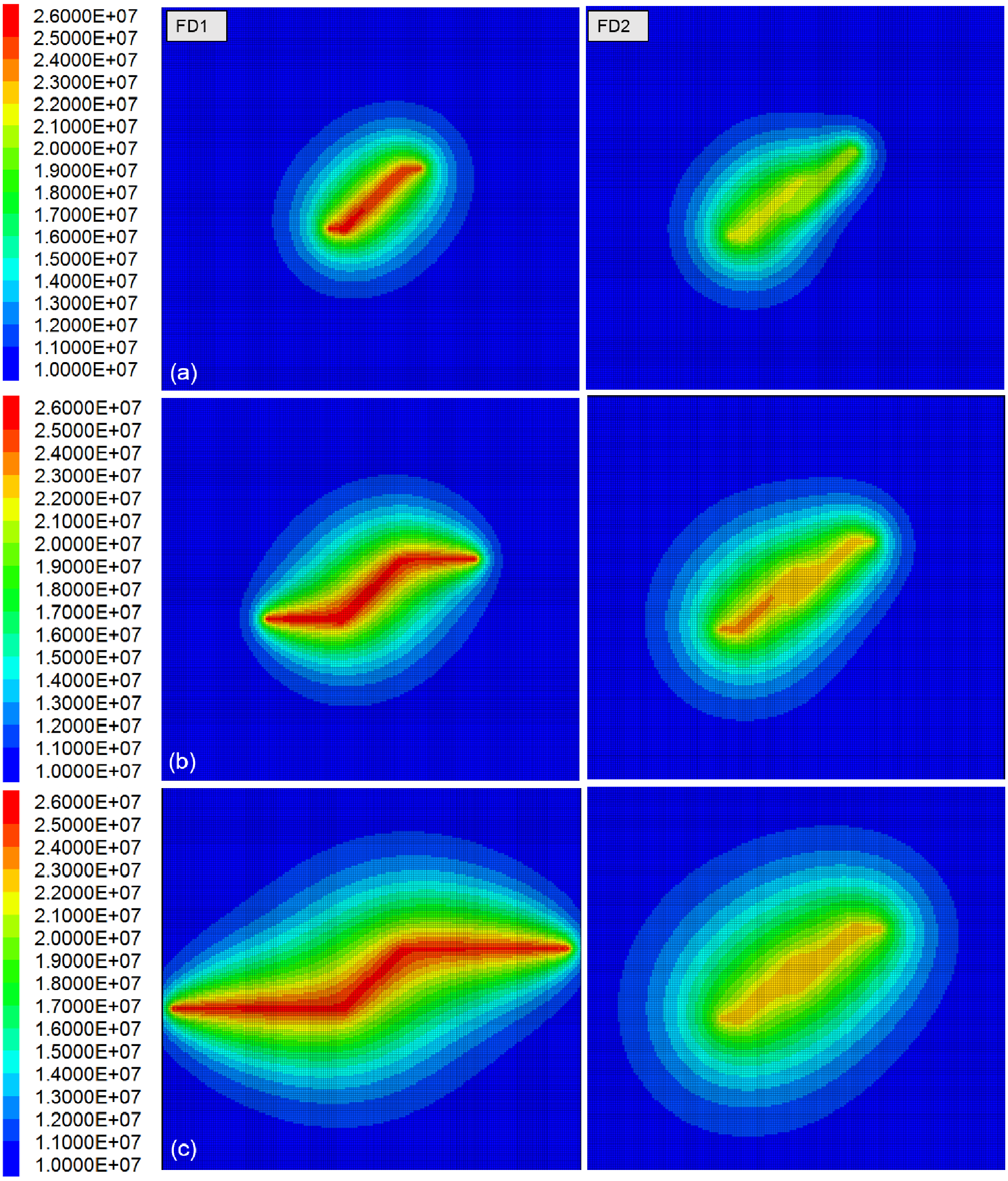

Fig. 10: Fluid pore pressure field (Pa) obtained over fractured rock domains FD1 (left) and FD2 with parallel fractures (right) for at (a) 1.5 hours (b) 2 hours and (c) 3 hours (results obtained for fracture angles α_1=α_2=45°)

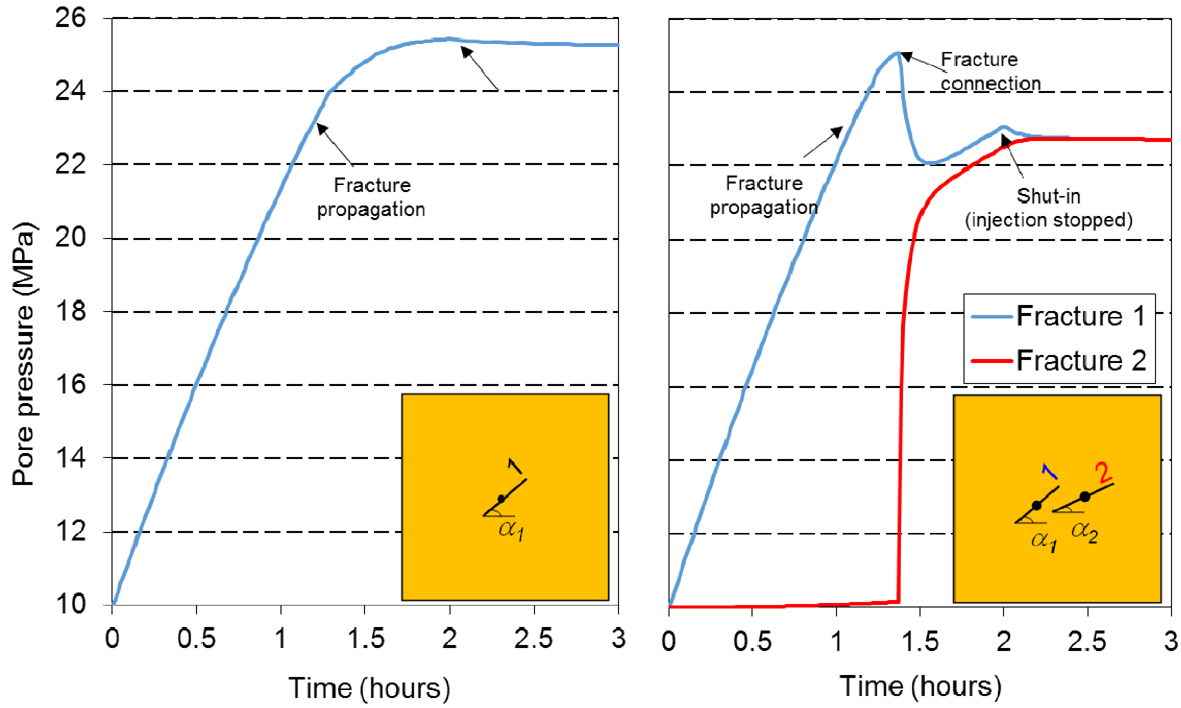

Fig. 11: Variation with time (hours) of the fluid pore pressure (MPa) in the centre of fractures for the fractured rock domains (left) FD1 and (right) FD2 with parallel fractures (results obtained for fracture angles α_1=α_2=45°)

Results show that the variation of fluid pore pressure with time in fractured rock domains FD1 and FD2 is different. In FD1, this relation is approximately linear until approximately 1 hour. The reason why this relation is not perfectly linear is because of the fluid pore pressure diffusion into the intact rock (see Fig. 10). For a fluid pore pressure of approximately 23 MPa, the fracture starts to propagate and the rate of fluid pore pressure build-up decreases with time. The fluid pore pressure necessary to initiate the fracture propagation is smaller than the minimum boundary stress magnitude (27 MPa). This is because the fracture has different properties from those of the surrounding intact rock, so that the minimum principal stress around the fracture tip gets slightly smaller than the minimum boundary stress magnitude, when differential boundary stresses are applied. The fracture starts to propagate when the tensile stress caused by pore pressure increase exceeds the tensile strength of the intact rock around the fracture tip. At that instant, the pore pressure at the fracture centre is larger than that at the tips. As the fracture propagates, the permeability of the elements failed by tension increases (see section 5.3). This leads to fluid penetration in the adjacent elements and a consequent increase in fluid pore pressure (see Fig. 10), which in turn, leads to tension failure in those elements. In this way, during the hydro-mechanical calculation, the fluid pore pressure diffusion follows the extension of the fractures (see Figs 8 and 10). At 1.5 and 2 hours of injection, the maximum fluid pore pressure in the fracture is 24.8 and 25.4 MPa. After shut-in, the pressure decrease is very small (less than 0.1 MPa) and the fracture propagates significantly at 3 hours (see Fig. 8).

In FD2, the fractures start to propagate approximately at the same fluid pore pressure as observed in FD1 (23 MPa). In fracture 1, the fluid pore pressure increases with time until the two fractures connect, which occurs after approximately 80 minutes and for a fluid pore pressure of about 25.5 MPa (see Fig. 11). Before the two fractures connect, there is a small increase of fluid pore pressure in fracture 2 (less than 0.2 MPa), due to the permeability of the intact rock. When the fractures connect, the fluid pore pressure in fractures 1 and 2 suddenly decreases and increases, respectively. At 1.5 hours of injection (10 minutes after the fractures connect), the fluid pore pressure in fractures 1 and 2 is approximately 22 and 21 MPa, respectively. After that, the fluid pore pressure continues to increase in both fractures because the increase in fractures permeability is not significant (see section 5.3) and the fracture 2 starts to propagate (see Fig. 8). At 2 hours of injection, the fluid pore pressure in fractures 1 and 2 is approximately 23 and 22.5 MPa. One hour after shut-in, the pore pressure in both fractures is significantly smaller than that observed in FD1 (approximately 22.8 MPa) and the fractures propagate only a further 0.15 m.

Fig. 12 shows the pore pressure field obtained at 2 hours of injection, for parallel fractures having angles $\alpha_1=\alpha_2$=30° and $\alpha_1=\alpha_2$=60°, and non-parallel fractures in which α_1=45°, α_2=30° and α_1=45°, α_2=60°. Fig. 13 shows the time evolution of pore pressure for those analysed four cases.

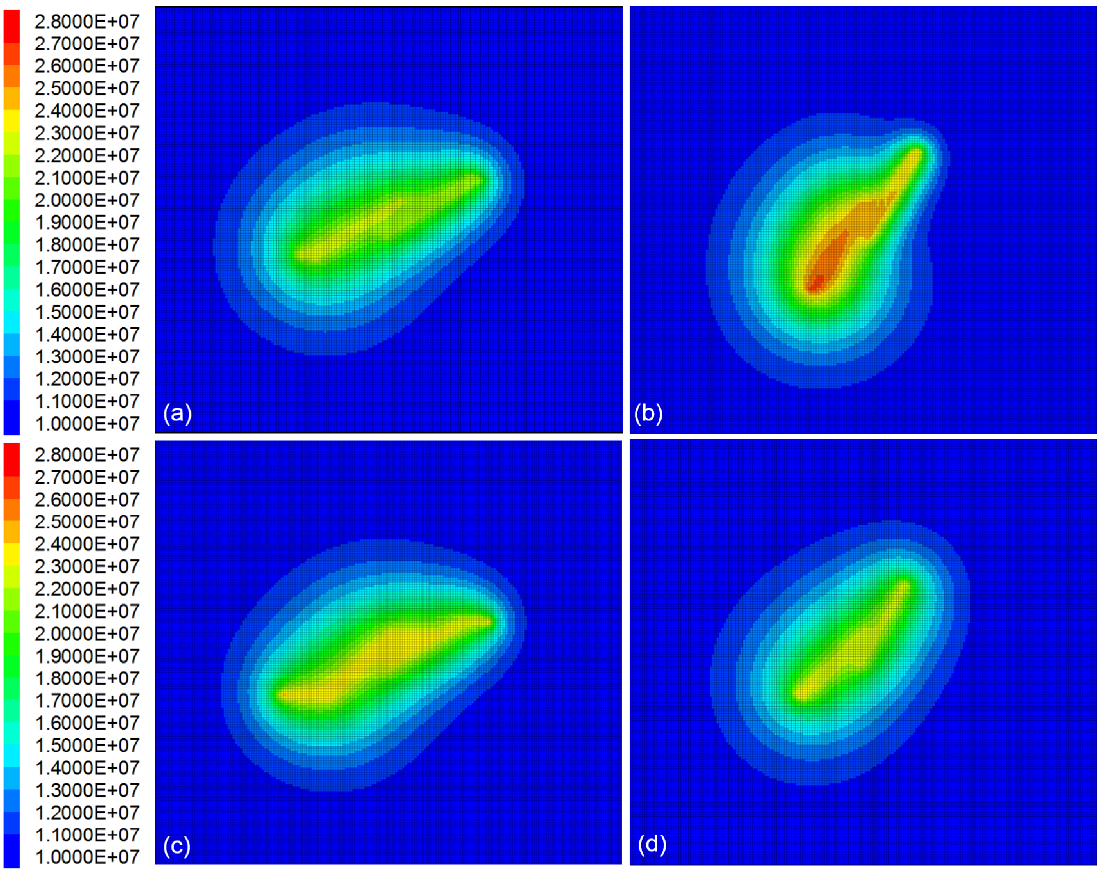

Fig. 12: Fluid pore pressure field (Pa) obtained over fractured rock domain FD2 for fracture angles (a) $\alpha_1=\alpha_2$ =30° (parallel) (b) $\alpha_1=\alpha_2$=60° (parallel) (c) α_1=45°, α_2=30° (non-parallel) (d) α_1=45°, α_2=60° (non-parallel) (results obtained at 2 hours of injection)

For parallel fractures, results obtained for $\alpha_1=\alpha_2$=30° show that the fractures connect when fluid pore pressure is similar to that obtained for $\alpha_1=\alpha_2$=45° (25.5 MPa). At 2 hours of injection, the fluid pore pressure in the two fractures is approximately equal to 23 MPa. When $\alpha_1=\alpha_2=60°$, the fluid pore pressure increases mainly in fracture 1 until the fractures connect for a maximum value of approximately 31.5 MPa, which is 6 MPa larger than that obtained when $\alpha_1=\alpha_2=30°$ or $\alpha_1=\alpha_2=45°$ (see Figs 11 and 13). For non-parallel fractures, results show that when the angle between the non-pressurised fracture (fracture 2) and the maximum boundary stress direction increases, the distance between the tip of the pressurised fracture and neighbouring fracture decreases and as a consequence, the time necessary for fractures to connect decreases. In this way, when the fractures connect at an earlier instant of time, the increase in the initial pore pressure is less and the fractures propagate less (see Fig. 9). The controlling factor appears to be the separation between the tips of the pressurised fracture 1 to the neighbouring fracture 2. This will be more discussed in section 6.1.

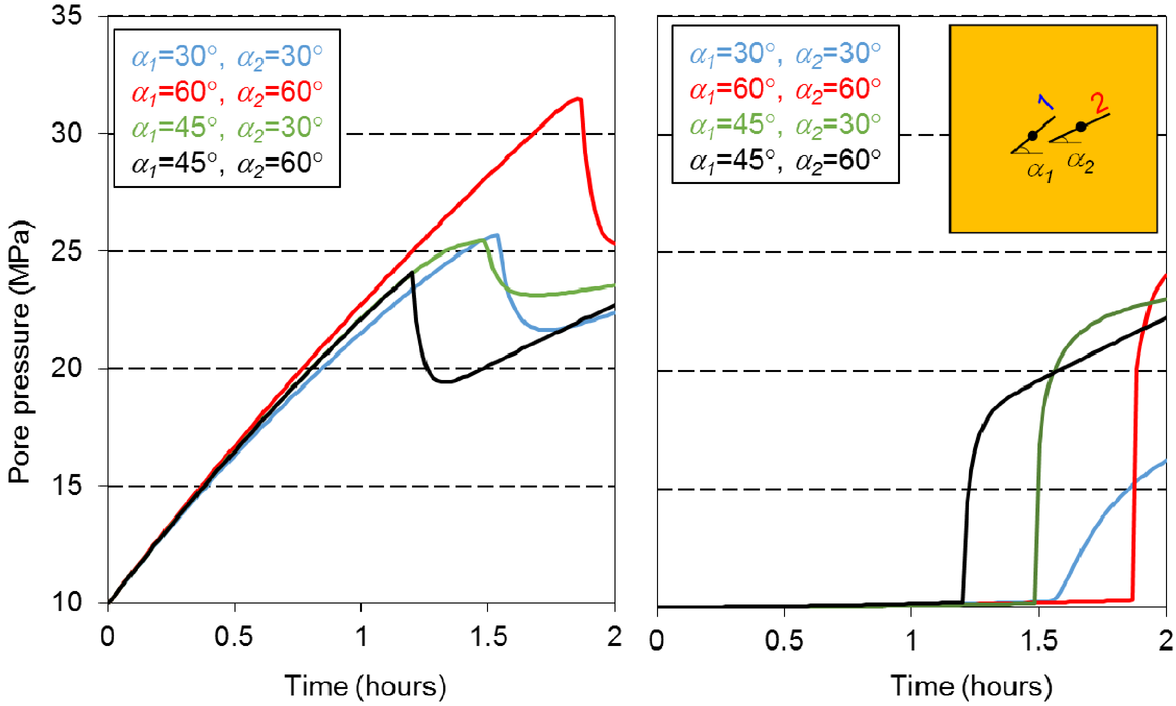

Fig. 13: Variation with time (hours) of the pore pressure (MPa) in the centre of the fractures 1 (left) and 2 (right) in fractured rock domain FD2, obtained for fracture angles α_1 and α_2 (results obtained at 2 hours of injection)

5.3 Changes in fracture permeability

In this section, changes in permeability of the fractures are analysed. Fig. 14 shows the variation with time of the permeability in the centre (points A and D) and tips (points B, C and E) of the fractures. These results were obtained for parallel fractures with angles $\alpha_1=\alpha_2=45°$.

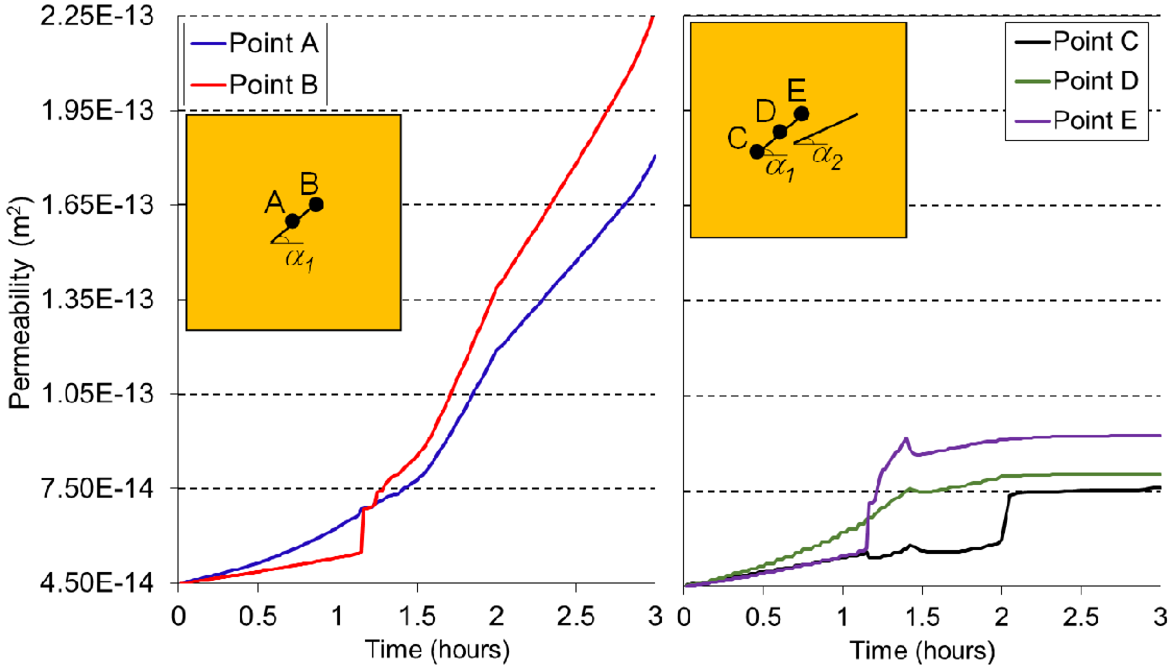

Fig. 14: Variation with time (hours) of the fracture permeability (m²) in the centre (points A and D) and tips (points B, C and E) of the fractures for the fractured rock domains FD1 (left) and FD2 (right) (results obtained for fracture angles α_1=α_2=45°)

In fractured rock domain FD1, it was found that before the fracture propagation initiates, changes in permeability in the centre of the fracture (point A) are slightly higher than those at the tip (point B). When the fracture starts to propagate, at approximately 70 minutes after injection is started, the increase in permeability at the fracture tip (point B) is larger than in the centre (point A). At 1.5 hours of injection, the permeability of the centre of the fracture (point A) is about 1.7 times the initial value. At 2 hours of injection, the maximum fracture permeability (point A) is approximately 3 times the initial value. After shut-in, the permeability of the fracture continues to increase because of changes in volumetric strains caused by fracture propagation. At 3 hours, the maximum fracture permeability (point B) is approximately 5 times the initial value. In FD2, changes in fracture permeability are less significant than in FD1 because when the two fractures become connected, the fluid pore pressure decreases (see Fig. 11) and as a result, changes in fractures aperture are smaller. After the fractures connect, the permeability at point E, located at the tip of the fracture, is slightly higher than at the centre (point D), as observed in FD1 case. At 2 hours of injection, in points D and E, the permeability is about 1.8 and 2.0 times the initial value, respectively. The fracture permeability remains practically constant after shut-in, because fracture propagation is very small (see Fig. 11).

Fig. 15 shows the time evolution of permeability in the centre of the fractures, for parallel fractures having angles α_1=α_2=30° and α_1=α_2=60° with the maximum boundary stress direction, and non-parallel fractures in which α_1=45°, and α_2=30° and α_2=60°. For parallel fractures, results obtained for α_1=α_2=30° show that the permeability changes are similar to those obtained with α_1=α_2=45° (see Fig. 14). As a result, the time evolution of pore pressure obtained with α_1=α_2=30° and α_1=α_2=45° is similar (see Figs 11 and 13). When α_1=α_2=60°, changes in permeability are the smaller than the other analysed cases. Although the injection pressure is larger than that in the other cases (see Fig. 13), the fracture propagates less because it is sub-perpendicular to the maximum principal direction (see Fig. 9). For the non-parallel fractures case, when α_2 increases from 30° to 60°, the permeability decreases because the fractures connect at an earlier time and as a result, the increase in the injection pore pressure is less (see Fig. 13), and the fracture propagation decreases.

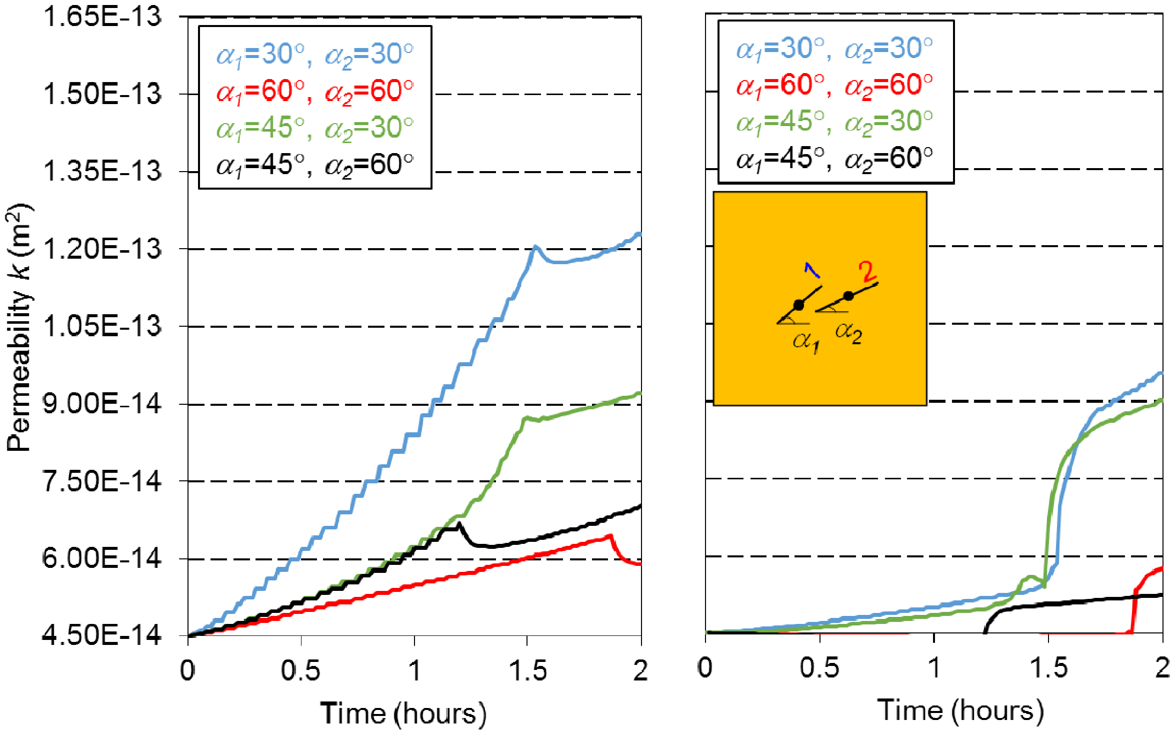

Fig. 15: Variation with time (hours) of the permeability (m^2) of in the centre of the fractures 1 (left) and 2 (right) in fractured rock domain FD2, obtained for fracture angles α_1 and α_2 (results obtained at 2 hours of injection)

6. SENSITIVITY ANALYSIS

This section presents the results of a sensitivity analysis to study the influence of the distance *d* between the fractures, the ratio *SR* between the magnitude of the maximum and minimum boundary stresses, the permeability k_R of the intact rock and the initial permeability k_{TF} of the tension failure regions, on the simulation results. The values of these key parameters used in the sensitivity study are presented in Table 2 together with those used for the base case. In this analysis, only fractured rock domain FD2 with parallel fractures inclined at an angle of 45° and the period up to shut-in (2 hours) were considered.

Table 2: Values of the key parameters considered in the base case and sensitivity study

Key parameter	Parameter value	
	Base case	Sensitivity study
Distance *d* (m)	0.25	0.50, 0.75
Stress ratio *SR*	0.7	0.6, 0.8
Permeability k_R (m^2)	10^{-18}	10^{-17} 10^{-16}
Initial fracture permeability k_{TF} (m^2)	4.5×10^{-14}	4.5×10^{-15} 4.5×10^{-16} 4.5×10^{-18}

6.1 Effect of the distance *d* between the fractures

Fig. 16 shows the fractures extension and the curves of variation of fluid pore pressure with time in the centre of fractures 1 and 2, obtained for a distance *d* between fractures of 0.5 m and 0.75 m. Results were compared with those presented in section 5, obtained for *d* equal to 0.25 m. When *d* increases from 0.25 m to 0.5 m, the fracture extension (away from the connection region) increases approximately 0.8 m. When *d* is 0.75 m, the propagation of fracture 1 is similar to that obtained in the single fracture case. This shows that as *d* increases the time necessary for fractures to connect slightly increases which leads to a major increase in pore pressure and propagation of the pressurised fracture. This results in a larger difference in fracture propagation and fluid pore pressure in the two fractures. In addition, as *d* increases the effects caused by the linkage between the two fractures decrease.

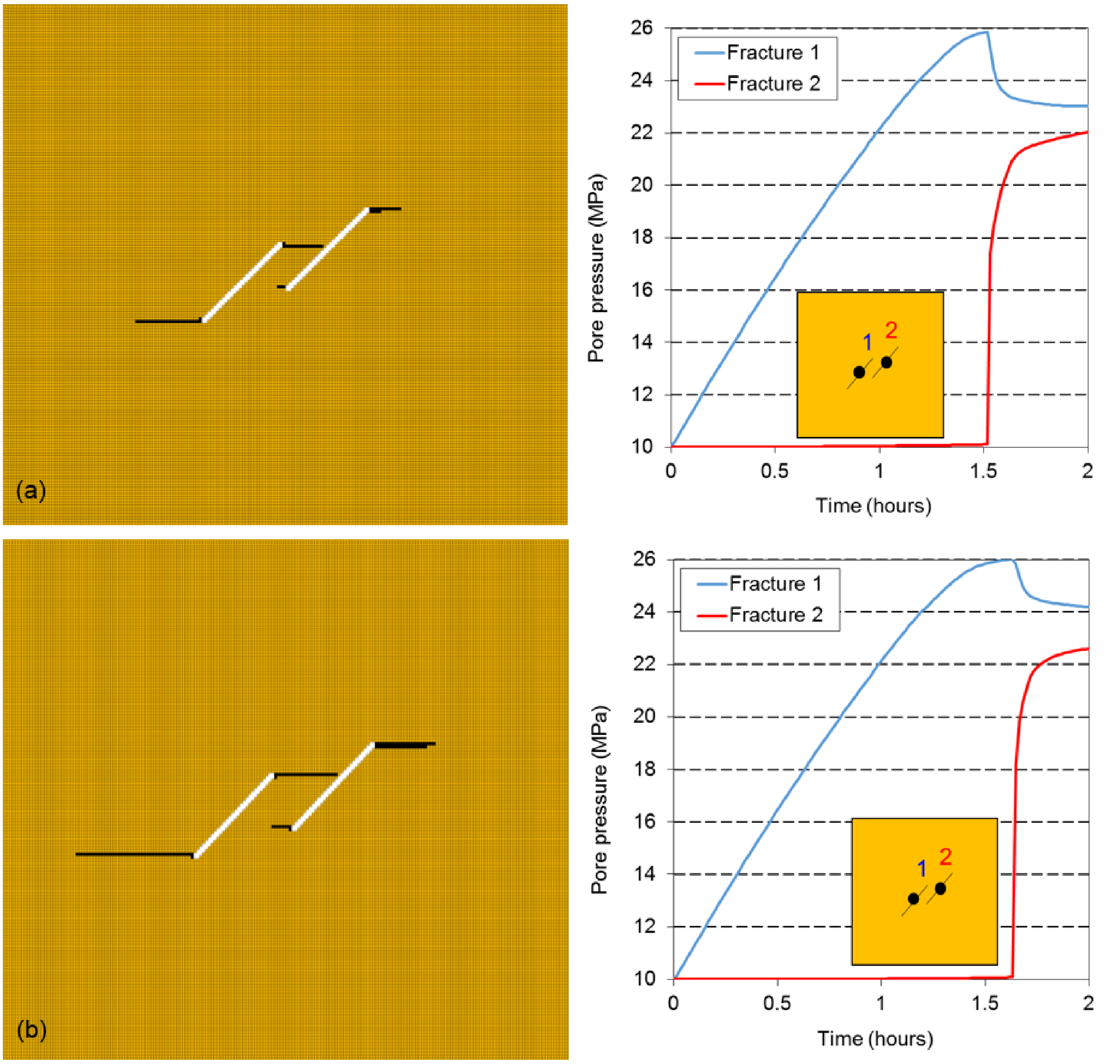

Fig. 16: Tension failure regions (left) and variation with time (hours) of fluid pore pressure (MPa) (right) obtained with d equal to (a) 0.50 m and (b) 0.75 m (results obtained at 2 hours of injection for fractured rock domain FD2 with fracture angles $\alpha_1=\alpha_2=45°$)

6.2 Effect of the ratio *SR* between the magnitudes of maximum and minimum horizontal stresses

Fig. 17 shows fracture extensions and fluid pore pressure field, obtained for *SR* equal to 1 and 3. Fig. 18 shows the variation with time of the fluid pore pressure in the centre of the fractures. Results obtained for S*R* equal to 1 show that the fractures do not propagate and hence, there is no interaction between the two fractures. Consequently, because the intact rock is less permeable than the fractures, the increase in fluid pore pressure in fracture 2 is negligible (less than 0.1 MPa). In fracture 1, the fluid pore pressure increases almost linearly with time during the injection period (see Fig. 18). At 2 hours of injection, the fluid pore pressure is approximately 32 MPa. Comparison with results presented for *SR* equal 2 enable us to conclude that the minimum fluid pore pressure necessary to extend the fractures increases when the boundary stresses have equal magnitude. In this case, to observe fracture propagation, the injection period has to be greater than 2 hours.

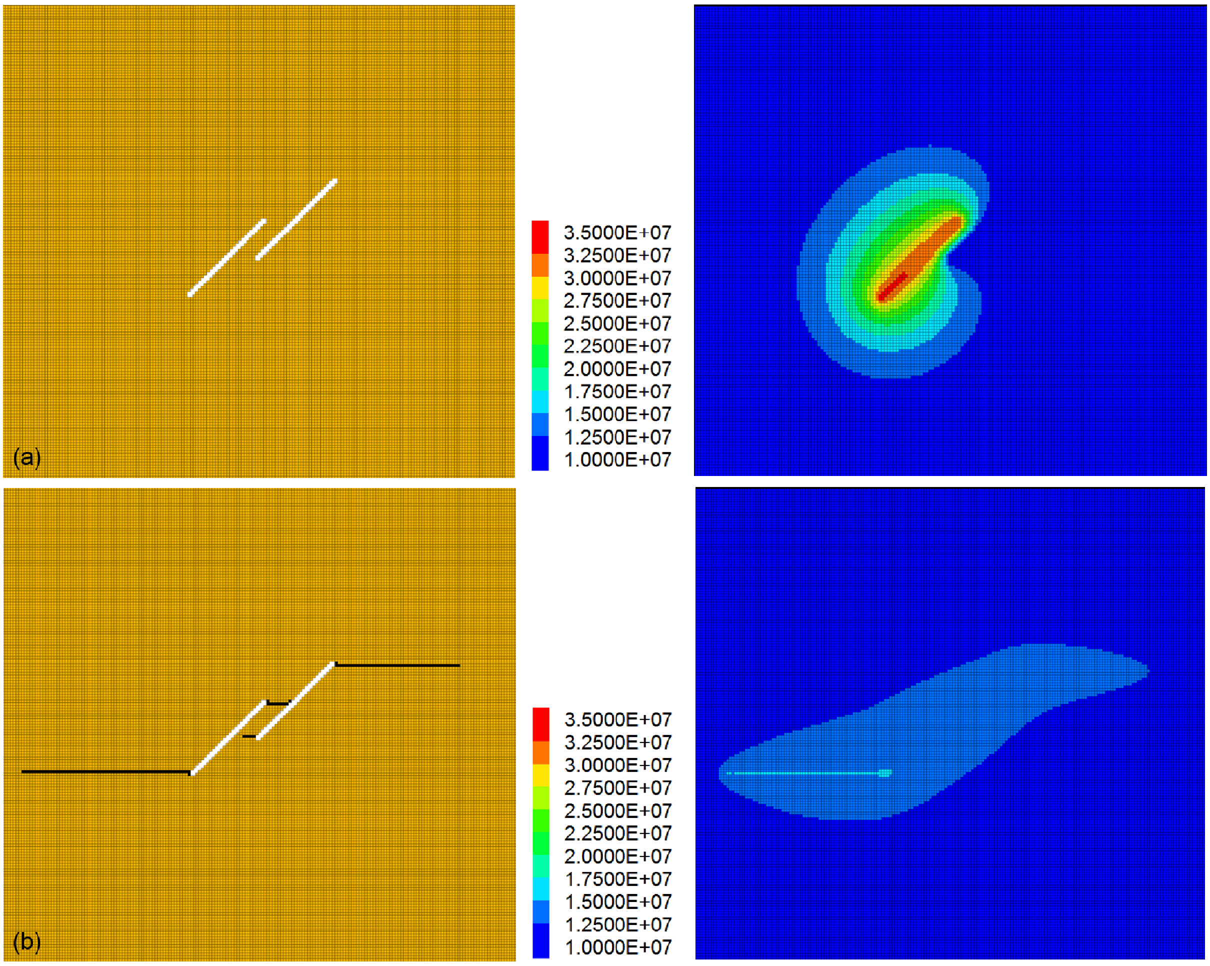

Fig. 17: Tension failure regions (left) and fluid pore pressure field (Pa) (right) obtained with a stress ratio *SR* equal to (a) 1 and (b) 3 (results obtained at 2 hours of injection for fractured rock domain FD2 with fracture angles α_1=α_2=45°)

When *SR* is equal to 3, the fractures propagate approximately 25 cm even before hydraulic fracturing stimulation starts. This fracture extension results already from stresses applied at the boundaries and an initial fluid pore pressure of 10 MPa. As a result, the rate of increase in fluid pore pressure with time is slower than that observed for *SR* equal to 1 and 2. In addition, because the principal stresses magnitude around the fracture tips decreases more for larger differential boundary stresses, the fractures connect for an injection pressure of significantly smaller (14.2 MPa) than the pressure of 25.5 MPa necessary for fractures to connect when *SR* is equal to 2 (see Fig. 11). After the fractures connect, the curves of the variation of fluid pore pressure with time are similar to those obtained for *SR* equal to 2. At 2 hours of injection, the fluid pore pressure in fractures 1 and 2 is approximately 14.6 and 14.2 MPa, respectively, and the fracture extension is approximately 3.65 m, which is 1.85 m more than that obtained for a stress ratio of 2 (see Figs 8 and 10). This shows the important role of the maximum principal stress magnitude on the propagation of existing fractures when they are stimulated by hydraulic fracturing.

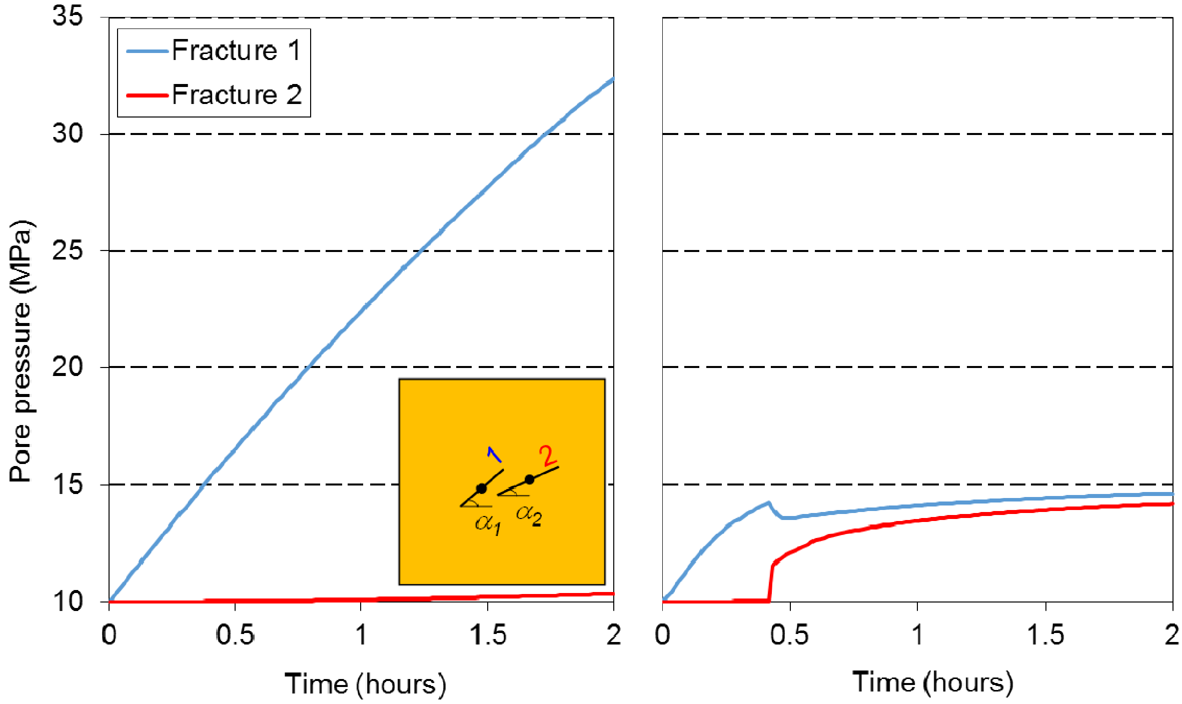

Fig. 18: Variation with time (hours) of the fluid pore pressure (MPa) in the centre of the fractures for fracture rock domain FD2 by considering a stress ratio *SR* of (left) 1 and (right) 3 (results obtained at 2 hours of injection for fractured rock domain FD2 with fracture angles α_1=α_2=45°)

6.3 Effect of permeability k_R of the intact rock

In this section, the influence of the permeability k_R of the intact rock on the simulation results, is analysed by considering two additional values for k_R: 10^{-17} and 10^{-16} m^2. Results for tension failure regions and fluid pore pressure field are presented in Fig. 19 and they were compared with those obtained for k_R equal to 10^{-18} m^2. Results show that when k_R increases by one order of magnitude, the fracture propagation decreases 15 cm. When k_R increases by two orders of magnitude, no fracture propagation is observed. The injection pressure decreases approximately 1 and 4.5 MPa when k_R increases by one and two orders of magnitude, respectively. This shows that as k_R increases the fracture propagation decreases because of the dissipating of pressure into the rock matrix and the resulting decrease in the pressure build-up around the fractures tip.

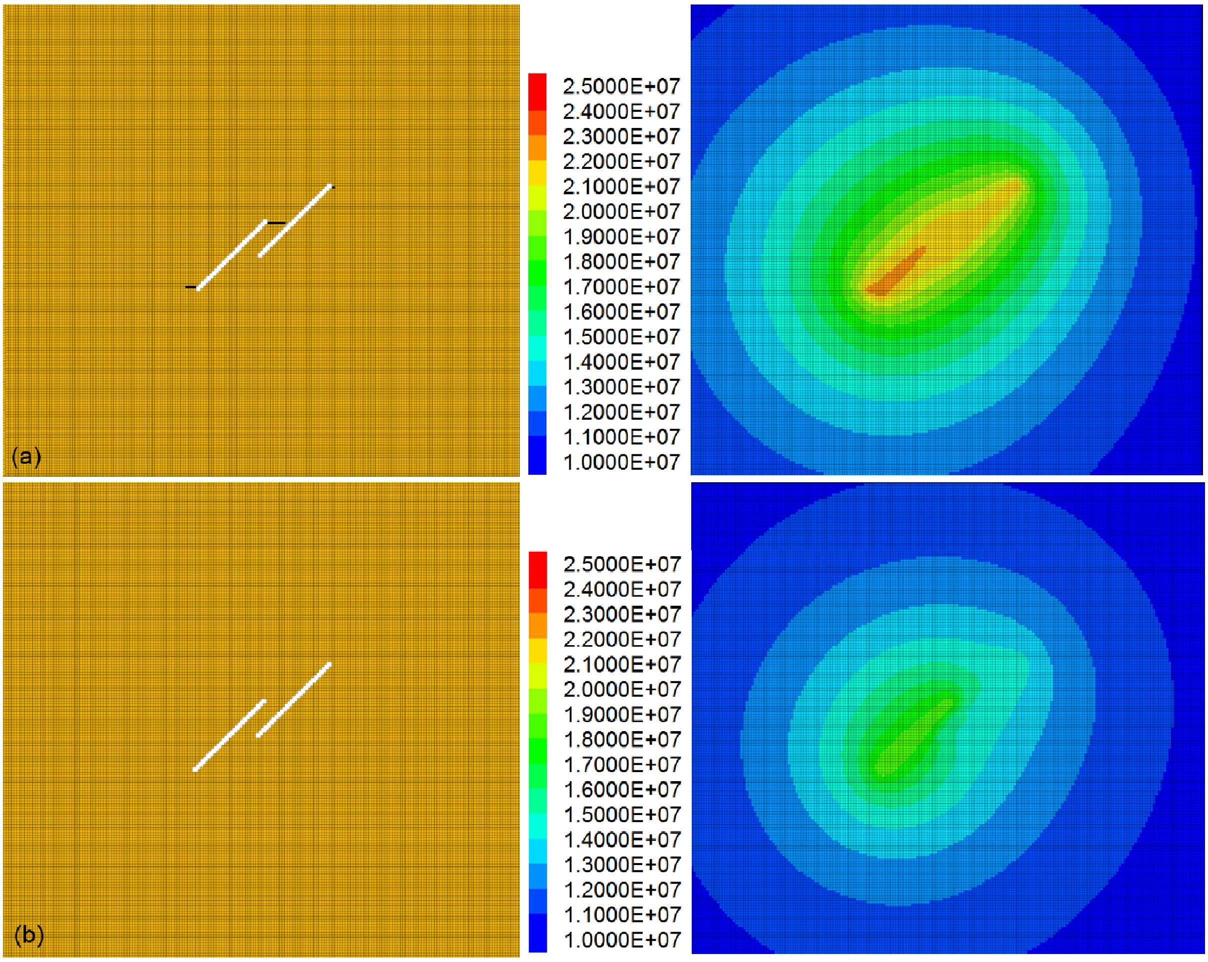

Fig. 19: Tension failure regions (left) and fluid pore pressure field (Pa) (right) obtained with a permeability k_R of the intact rock equal to (a) 10^{-17} m^2 (b) 10^{-16} m^2 (results obtained at 2 hours of injection for fractured rock domain FD2 with fracture angles α_1=α_2=45°)

6.4 Effect of the initial permeability k_{TF} of the tension failure regions

Fig. 20 shows the fractures extension and fluid pore pressure field, obtained for an initial permeability k_{TF} of the failure regions equal to 4.5×10^{-15} m^2, 4.5×10^{-16} m^2 and 4.5×10^{-18} m^2. Results show that when k_{TF} decreases one order of magnitude from 4.5×10^{-14} m^2 to 4.5×10^{-15} m^2, the extension of fractures 1 and 2 decreases approximately 10 and 25 cm, respectively. The difference between the maximum values in fluid pore pressure observed at the centre of the two fractures increases from 0.6 to 2.1 MPa. This is because as k_{TF} decreases, it is more difficult for fluid to penetrate into the recently created fracture and hence, the fluid pore pressure increases more in the fracture where hydraulic fracturing occurs. When k_{TF} decreases by two orders of magnitude, this difference in fluid pore pressure in the two fractures increases to 4.7 MPa, and the propagation of fracture 2 is only 10 cm. In contrast, fracture 1 propagation increases by 0.55 m. When k_{TF} is set to 4.5×10^{-18} m^2, fracture 1 propagates 15 cm more than in the case of k_{TF} equal to 4.5×10^{-16} m^2, but fracture 2 does not propagate. Because of the changes in volumetric strains, the permeability of the tension failure elements increases by two orders of magnitude with respect to their initial permeability k_{TF}. This is not enough to lead to significant flow in fracture 2, and the difference in fluid pore pressure between fractures 1 and 2 increases to

20 MPa. In this case, practically there is no fluid pore pressure build-up in fracture 2. This concludes that results are more sensitivity to the initial permeability k_{TF} of the failure regions than to changes in volumetric strains in the elements subjected to tension failure.

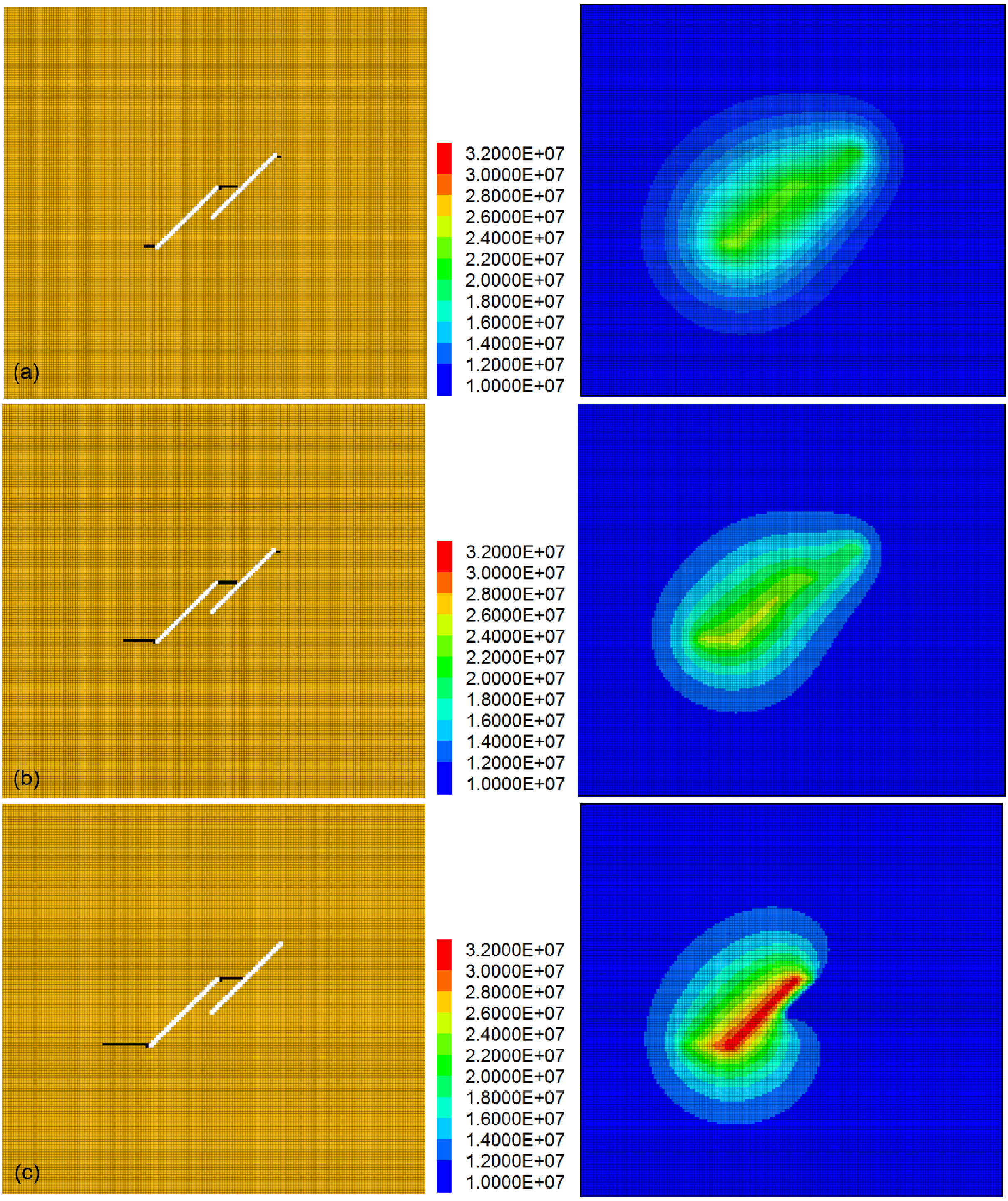

Fig. 20: Tension failure regions (left) and fluid pore pressure field (Pa) (right) obtained with a permeability k_{TF} of the tension failure regions equal to (a) 4.5×10^{-15} m^2 (b) 4.5×10^{-16} m^2 and (c) 4.5×10^{-18} m^2 (results obtained at 2 hours of injection for fractured rock domain FD2 with fracture angles $\alpha_1=\alpha_2=45°$)

7. CONCLUDING REMARKS

The focus of the present study is on the influence of a neighbouring fracture on a fracture subjected to increased fluid pressure during hydraulic fracturing stimulation. This is accomplished by a comparative coupled hydro-mechanical analysis of two fractured rock domains: FD1, with one single fracture; and FD2, with two adjacent parallel and non-parallel fractures. Hydraulic fracturing was assumed to occur by high-pressure injection in the single fracture in FD1 and one of the two fractures in FD2. Simulations were made for a time period of 3 hours with an injection period of 2 hours. A base case was considered in which the closest distance *d* between the two fractures is 0.25 m, the ratio *SR* between the magnitude of the maximum and minimum boundary stresses is set to be 2, the permeability k_R of the intact rock is set to be 10^{-18} m^2 and the initial permeability k_{TF} of the tension failure regions is considered to be equal to the initial permeability of the natural fractures. The conclusions from the obtained results may be summarized as follows:

Firstly, the minimum fluid pore pressure necessary to initiate fractures propagation is smaller than the minimum boundary stress magnitude (approximately 85%). This is because the fractures have softer properties than the intact rock, and due to boundary stresses, the minimum principal stress at the tips is smaller than the minimum boundary stress magnitude. The fractures start to propagate when the local tensile stress around the tip of the fracture, induced by increase in pore pressure, is larger than the tensile strength of the intact rock. At that instant, the pore pressure at its centre is larger than that at the tip of the fracture. It was found that until the fractures start to propagate, the injection pressure increases with time, but this relation is not perfectly linear because of fluid pore pressure diffusion into the permeable intact rock. In contrast with the FD1 case, in the case of FD2 the pressure in the pressurised fracture decreases significantly (approximately 15%) after it connects to the second fracture.

Secondly, in a double fractures case, with parallel fractures, the results obtained with an angle between the two fractures and the maximum principal stress direction (horizontal) of 30° and 45°, were found to be similar. However, when the fractures are inclined at an angle of 60°, they are sub-perpendicular to the maximum principal stress direction, and hence, the propagation of fractures is smaller. The fractures will connect after an injection period larger than that observed for an angle equal to 30° or 45°, and as a result, in the former case, the fluid pore pressure increases more in the fracture subjected to water injection. When the fractures are non-parallel, it was found that, as the angle between the non-pressurised fracture and the maximum boundary stress direction increases, the time necessary for fractures to connect decreases, the increase in pore pressure is less, and hence the fracture propagation decreases.

Thirdly, the propagation of a single fracture caused by water injection is larger than that obtained with the presence of a neighbouring second fracture. This is because in the latter case, the pore pressure decreases when the two fractures connect and the tensile stress at the tip of fracture is then not enough exceed the tensile strength of the intact rock.

Fourthly, in a single fracture case, changes in fracture permeability were found to be larger than those obtained in a double fractures case. This is because in the latter case, the injection pressure decreases when the fractures connect, and thus changes in the fractures aperture are smaller than in the former case. However, changes in fracture permeability were found to be not very significant. At 2 hours of injection, the maximum ratio between the final and initial fracture permeability was approximately 3. Consequently, after the fractures start to propagate, the injection pressure still increases.

A sensitivity study was made to analyse the influence of the key parameters referred above on the obtained results for the particular case of FD2 with parallel fractures inclined at an angle of 45°. It is found that:

1. When the distance *d* between the two fractures increases, the pressurised fracture extends more and the effect of linkage between fractures on their propagation decreases. At the limit, for a very large *d* value, the results obtained for the single and double fractures case are expected to be very similar.
2. When the ratio *SR* between the boundary stresses magnitude increases, the minimum fluid pore pressure value necessary to initiate fracture propagation decreases. This is because when *SR* increases, the minimum principal stress around the fracture tip decreases.
3. When the permeability k_R of the intact rock increases, the pore pressure around the fracture tip decreases, which results in a decrease in the fracture propagation. On the other hand, it was found that when k_{TF} decreases, the fractures may connect but the difference in fluid pore pressure observed in the two fractures increases. This is because when the tension failure regions are more impermeable, the flow between the two fractures is less. This shows that differences in results are more sensitive to the initial permeability of the tension failure regions than to stress induced changes in their apertures.

To summarise, fracture propagation was found to be more sensitive to *d* and *SR* than to the other parameters. The conclusions from the present study bring out some interesting aspects of fracture rock hydromechanics that deserve further studies and these need to be accounted for in modelling hydro-mechanical behaviour of fractured rocks during a hydraulic fracturing operation. As further work it is proposed to apply the methodology presented in this paper to study the fractured propagation in the three dimensional space and also when the multi-phase fluid is involved.

ACKNOWLEDGMENTS

The authors gratefully acknowledge the Swedish Geological Survey (SGU), grant number 1724, and the EU project, grant number 640979, for providing financial support to research reported in this paper. Additional support was provided by the U.S. Department of Energy under contract No. DE-AC02-05CH11231.

REFERENCES

[1] Min KB, Rutqvist J, Tsang CF, Jing L. Stress-dependent permeability of fractured rock masses: a numerical study. Int. J. Rock Mech. Min. Sci. 2004; 41: 1191-1210.

[2] Rutqvist J, Stephansson O. The role of hydro-mechanical coupling in fractured rock engineering. Hydrogeology J. 2013; 11: 7-40.

[3] Tsang CF, Niemi A. Deep hydrogeology: a discussion of issues and research needs. Hydrogeology J. 2013; 21: 1687-90.

[4] Germanovich LN, Astakhov DK. Stress-dependent permeability and fluid flow through parallel joints. J. Geophys. Res. 2004; 108: doi:10.1029/2002JB002133, in press.

[5] Germanovich L, Askakhov D. Fracture closure in extension and mechanical interaction of parallel joints. J. Geophys. Res. 2004; 109: B02208, doi: 10.1029/2002JB002131.

[6] Germanovich LN, Ring LM, Astakhov DK, Shlyapobersky J, Mayerhofer MJ. Hydraulic fracture with multiple segments, part II: Effect of interaction. Int. J. Rock Mech. Min. Sci. Geomech. Abstr. 1997; 34 (3): 98.e1–98.e15.

[7] Reyes O. Experimental Study and Analytical Modeling of Compressive Fracture in Brittle Materials (Ph.D. thesis). Massachusetts Institute of Technology, 1991.

[8] Bobet A, Einstein HH. Fracture coalescence in rock-type materials under uniaxial and biaxial compression. Int. J. Rock Mech. Min. Sci. 1998; 35 (7): 863–88.

[9] Wong LNY, Einstein HH. Crack coalescence in molded gypsum and Carrara marble: part 1 – Macroscopic observations and interpretation. Rock Mech. Rock Eng. 2009a; 42 (3): 475–511.

[10] Wong LNY, Einstein HH. Crack coalescence in molded gypsum and Carrara marble: part 2 – macroscopic observations and interpretation. Rock Mech. Rock Eng. 2009b; 42 (3): 513–45.

[11] Miller JT. Crack coalescence in granite (S.M. thesis). Massachusetts Institute Technology, 2008.

[12] Morgan S, Johnson C, Einstein H. Cracking processes in Barre granite: fracture process zones and crack coalescence. Int. J. Fract. 2013; 180: 177–204.

[13] Zang A, Wagner C, Stanchits S, Dresen G, Andresen R, Haidekker M. Source analysis of acoustic emissions in Aue granite cores under symmetric and asymmetric compressive loads. Int. J. Geophys. 1998; 135: 1113–30.

[14] Mayer SI, Stanchits S, Langenbruch C, Dresen G, Shapiro S. Acoustic emission induced by pore-pressure changes in sandstone samples. Geophysics 2011; 76 (3): MA21–MA32.

[15] Ramulu M, Kobayashi AS. Mechanics of crack curving and branching – a dynamic fracture analysis. Int. J. Fract. 1985; 27: 187–201.

[16] Guo ZK, Kobayashi AS. Dynamic mixed mode fracture of concrete. Int. J. Solids Struct. 1995; 32: 2591–07.

[17] Ravi-Chandar K. Fracture Dynamics. Elsevier B.V, Amsterdam, 2004.

[18] Moes N, Belytschko T. A finite element method for growth without remeshing. Int. J. Numer. Meth. Eng. 1999; 46 (1): 131–50.

[19] Mughieda O, Omar MT. Stress analysis for rock mass failure with offset joints. Geotech. Geol. Eng. 2008; 26: 543–52.

[20] Gonçalves da Silva B, Einstein HH. Modeling of crack initiation, propagation and coalescence in rocks. Int. J. Fract. 2013; 182 (2): 167–86.

[21] Li HQ, Wong LNY. Influence of flaw inclination angle and loading condition on crack initiation and propagation. Int. J. Solids Struct. 2012; 49: 2482–99.

[22] Yao Y. Linear elastic and cohesive fracture analysis to model hydraulic fracture in brittle and ductile rocks. Rock Mech. Rock Eng. 2012; 45: 375–87.

[23] Lecampion B. An extended finite element method for hydraulic fracture problems. Commun. Numer. Meth. Engng 2009; 25: 121-33.

[24] Rannou J, Limodin N, Réthoré J, Gravouil A, Ludwig W, Baïetto-Dubourg MC, Buffière JY, Combescure A, Hild F, Roux S. Three dimensional experimental and numerical multiscale analysis of a fatigue crack. Comput. Meth. Appl. Mech. Eng. 2010; 199 (21–22): 1307– 25.

[25] Liu ZL. An XFEM/Spectral element method for dynamic crack propagation. Int. J. Fract. 2011; 169: 183–98.

[26] Xu Y, Yuan H. Applications of normal stress dominated cohesive zone models for mixed-mode crack simulation based on the extended finite element methods. Eng. Fract. Mech. 2011; 78: 544–58.

[27] Fang Z, Harrison JP. Development of a local degradation approach to the modeling of brittle fracture in heterogeneous rocks. Int. J. Rock Mech. Min. Sci. 2002; 39: 443–57.

[28] Fang Z, Harrison JP. Application of a local degradation model to the analysis of brittle fracture of laboratory scale rock specimens under triaxial conditions. Int. J. Rock Mech. Min. Sci. 2002; 39: 459–76.

[29] Li Y, Zhou H, Zhu W, Li S, Liu J. Numerical study of crack propagation in brittle joined rock mass influenced by fracture water pressure. Materials 2015; 8: 3364-76.

[30] Bobet A, Einstein HH. Numerical modeling of fracture coalescence in a model rock material. Int. J. Fract. 1998a; 92: 221–52.

[31] Vásárhelyi B, Bobet A. Modelling of crack initiation, propagation and coalescence in uniaxial compression. Rock Mech. Rock Eng. 2000; 33 (2): 119-39.

[32] Gonçalves da Silva B, Einstein HH. Modeling of crack initiation, propagation and coalescence in rocks. Int. J. Fract. 2013: 182 (2): 167–86.

[33] Potyondy DO, Cundall PA. A bonded-particle model for rock. Int. J. Rock Mech. Min. Sci. 2004; 41: 1329–64.

[34] Yoon J. Application of experimental design and optimization to PFC model calibration in uniaxial compression simulation. Int. J. Rock Mech. Min. Sci. 2007; 44: 871–89.

[35] Lee H, Jeon S. An experimental and numerical study of fracture coalescence in pre-cracked specimens under uniaxial compression. Int. J. Solids Struct. 2011; 48: 979-99.

[36] Jia L, Chen M, Zhang W, Xu T, Zhou Y, Hou B, Yan J. Experimental study and numerical modeling of brittle fracture of carbonate rock under uniaxial compression. Mech. Res. Commun. 2013; 50: 58–62.

[37] Yang SQ, Huang YH, Jing HW, Liu XR. Discrete element modeling on fracture coalescence behavior of red sandstone containing two unparallel fissures under uniaxial compression. Eng. Geol. 2014; 178: 28–48.

[38] Manouchehrian A, Sharifzadeh M, Marji MF, Gholamnejad J. A bonded particle model for analysis of the flaw orientation effect on crack propagation mechanism in brittle materials under compression. Arch. Civ. Mech. Eng. 2014; 14: 40–52.

[39] Zhang X and Sanderson D. Evaluation of instability in fractured rock masses using numerical analysis methods: Effects of fracture geometry and loading direction. J. Geophys. Res. 106 (B11): 26671-687.

[40] Pearce CJ, Thavalingam A, Liao Z, Bićanić N. Computational aspects of the discontinuous deformation analysis framework for modelling concrete fracture. Eng. Fract. Mech. 2000; 65: 283–98.

[41] Rutqvist J, Leung C, Hoch A, Wang Y, Wang Z. Linked multicontinuum and crack tensor approach for modeling of coupled geomechanics, fluid flow and transport in fractured rock. Journal of Rock Mechanics and Geotechnical Engineering. 2013; 5: 18-31.

[42] Settari A, Sullivan RB, Walters DA, Wawrzynek PA. 3-D analysis and prediction of microseismicity in fracturing by coupled geomechanical modeling. Society of Petroleum Engineers 2002. Paper 75714. http://www.onepetro.org/conference-paper/SPE-75714-MS.

[43] Ji LJ, Settari A, Sullivan R. A novel hydraulic fracturing model fully coupled with geomechanics and reservoir stimulation. Soc. Pet. Eng. J. 2009; 14 (3): 423–30.

[44] Hou ZM, Zhou L, Kracke T. Modelling of seismic events induced by reservoir stimulation in an enhanced geothermal system and a suggestion to reduce the deformation energy release. Rock Dynamics and Applications – State of the Art. Taylor and Francis Group, London, United Kingdom (pp. 161–175), 2013.

[45] Wangen M. Finite element modeling of hydraulic fracturing in 3D. Comput. Geosci. 2013; 17 (4): 647–59.

[46] Yarushina VM, Bercovici D, Oristaglio M. Rock deformation models and fluid leak-off in hydraulic fracturing. Geophys. J. Int. 2013; 194 (3): 1514–26.

[47] Itasca. FLAC3D, Version 5.0. User's Manual. Itasca Consulting Group, Minneapolis; 2012.

[48] Pruess K, Oldenburg C, Moridis G. TOUGH2 user's guide, version 2.0, Lawrence Berkeley National Laboratory Report, LBNL-43134, Berkeley, p.198; 2011.

[49] Figueiredo B, Tsang CF, Rutqvist J, Niemi A. A study of changes in deep fractured rock permeability due to coupled hydro-mechanical effects. Int. J. Rock Mech. Min. Sci. 2015; 79: 70-85.

[50] Cappa F, Rutqvist J. Modeling of coupled deformation and permeability evolution during fault reactivation induced by deep underground injection of CO_2. Int. J. Greenhouse Gas Control 2011; 5: 336-46.

[51] Attewell PB, Farmer IW. Principles of engineering geology. John Wiley & Sons Inc., New York; 1976.

[52] Zhao J. Properties of rock materials. In: Rock mechanics for civil engineering, www.epf.ch/en/ensei/Rock-Mechanics/ENS-080312-EN-Notes-Chapter-4.pdf. 2008. 49 p.

[53] Chin LY, Raghavan R, Thomas LK. Fully coupled geomechanics and fluid flow analysis of wells with stress-dependent permeability. Soc. Petrol. Eng. 2000; 5: 32-45.

[54] Rinaldi A, Rutqvist J, Cappa F. Geomechanical effects of CO_2 leakage through fault zones during large-scale underground injection. Int. J. Greenhouse Gas Control 2014; 20: 117-31.

[55] Witherspoon PA, Wang JSY, Iwai K, Gale JE. Validity of cubic law for fluid flow in a deformable rock fracture. Water Resour. Res. 1980; 16: 1016-24.

[56] Mutlu O, Pollard D. On the patterns of wing crack along an outcrop scale flaw: a numerical modeling approach using complementarity. J. Geophy. Res. 2008; 113: B06403, doi: 10.1029/2007JB005284.

[57] Pollard DD, Segall P. Theoretical displacements and stresses near fractures in rock: with applications to faults, joints, veins, dikes, and solution surfaces. In: Fracture mechanics of rock, BK Atkinson, editor. Academic Press Inc; 1987. pp. 277-349.